



## Flow condensation pressure oscillations at different orientations

Lucas E. O'Neill<sup>a</sup>, Issam Mudawar<sup>a,\*</sup>, Mohammad M. Hasan<sup>b</sup>, Henry K. Nahra<sup>b</sup>,  
R. Balasubramaniam<sup>b</sup>, Jeffery R. Mackey<sup>c</sup>

<sup>a</sup> Purdue University Boiling and Two-Phase Flow Laboratory (PU-BTPFL), School of Mechanical Engineering, Purdue University, 585 Purdue Mall, West Lafayette, IN 47907, USA

<sup>b</sup> NASA Glenn Research Center, 21000 Brookpark Road, Cleveland, OH 44135, USA

<sup>c</sup> Vantage Partners, 3000 Aerospace Parkway, Brook Park, OH 44142, USA



### ARTICLE INFO

#### Article history:

Received 14 May 2018

Received in revised form 9 July 2018

Accepted 12 July 2018

Available online 30 July 2018

#### Keywords:

Flow condensation

Flow instabilities

Pressure oscillations

Frequency and amplitude

### ABSTRACT

Investigation of two-phase flow dynamic behavior and instabilities has traditionally centered on phenomena present in boiling flows due to the safety critical nature of boiling in a variety of cooling applications. Analysis of pressure signals in condensing systems reveal the presence of relevant oscillatory phenomena during flow condensation as well, which may impact performance in applications concerned with precise system control. Towards this end, the present study presents results for oscillatory behavior observed in pressure measurements during flow condensation of FC-72 in a smooth circular tube in vertical upflow, vertical downflow, and horizontal flow orientations. Dynamic behavior observed within the test section is determined to be independent of other components within the flow loop, allowing it to be isolated and interpreted as resulting from physical aspects of two-phase flow with condensation. The presence of a peak oscillatory mode (one of significantly larger amplitude than any others present) is seen for 72% of vertical upflow test cases, 61% of vertical downflow, and 54% of horizontal flow. Relative intensities of this peak oscillatory mode are evaluated through calculation of Q Factor for the corresponding frequency response peak. Frequency and amplitude of peak oscillatory modes are also evaluated. Overall, vertical upflow is seen to exhibit the most significant oscillatory behavior, although in its maximum case amplitude is only seen to be 7.9% of time-averaged module inlet pressure, indicating there is little safety risk posed by oscillations under current operating conditions. Flow visualization image sequences for each orientation are also presented and used to draw parallels between physical characteristics of condensate film behavior under different operating conditions and trends in oscillatory behavior detected in pressure signals.

© 2018 Elsevier Ltd. All rights reserved.

## 1. Introduction

### 1.1. Importance of flow condensation dynamic behavior

A key trend across all energy applications in recent years has been that of miniaturization coupled with increased capacity. System modifications following these trends have led to increased performance and smaller size, both advantageous features from product design standpoints. From a heat transfer perspective, however, this leads to a necessity of higher flux thermal management systems to reject heat [1].

To satisfy these increasingly stringent thermal management requirements, engineers have begun turning to schemes relying on phase change heat transfer. These systems typically rely on

boiling to acquire heat from the device being cooled and condensation to reject heat from the working fluid and return it to a pre-boiling (subcooled or saturated liquid) state. Many prior studies have investigated boiling through a variety of mechanisms, including capillary-driven devices [2–4], pool boiling thermosyphons [5–7], falling film [8,9], channel flow boiling [10,11], micro-channel boiling [12–16], jet impingement [17–20], and spray [21–27], as well as hybrid configurations [28–31] involving two or more of these schemes. Similarly, condensation has been investigated in several configurations, including falling film [32–34], flow through single circular mini-channels [35–41], and flow through parallel micro-channel arrays [42–44]. A common deficiency found across most studies on condensation, however, is lack of emphasis on transient flow behavior and analysis of potential instability modes brought on by the condensation process.

Transient flow behavior is particularly important for aerospace applications (for which phase change thermal management systems are attractive due to their ability to offer superior heat

\* Corresponding author.

E-mail address: [mudawar@ecn.purdue.edu](mailto:mudawar@ecn.purdue.edu) (I. Mudawar).

URL: <https://engineering.purdue.edu/BTPFL> (I. Mudawar).

**Nomenclature**

$A$	amplitude
$c_p$	specific heat at constant pressure
$D$	diameter
$D_h$	hydraulic diameter
$f$	frequency
$Fr$	Froude number
$G$	mass velocity
$g$	Earth's gravitational constant
$H$	digital filter transfer function
$h_{fg}$	latent heat of vaporization
$\dot{m}$	mass flow rate
$P$	pressure
$P'$	mean-subtracted pressure fluctuations
$P_{wv}$	power input
$Q$	Q Factor, measure of oscillatory mode intensity
$Re$	Reynolds number
$T$	temperature
$t$	time
$We$	Weber number
$x_e$	thermodynamic equilibrium quality
$z$	variable indicating digital domain; stream-wise position
<i>Greek symbol</i>	
$\mu$	dynamic viscosity
$v$	specific volume
$\rho$	density
$\sigma$	surface tension

*Subscripts*

$A$	amplitude
<i>ave</i>	average
$BH$	bulk heater
$f$	saturated liquid
$FC$	FC-72, condensate
$FWHM$	full width half maximum
$g$	saturated vapor
$H_2O$	water, cooling fluid
$i$	inner (refers to diameter)
$in$	inlet to condensation length (refers to condensate)
$max$	max value over range evaluated
$mean$	mean value over range evaluated
$o$	outer (refers to diameter)
$out$	outlet to condensation length (refers to condensate)
$P$	pressure

*Acronyms*

CM-FV	condensation module for flow visualization
CM-HT	condensation module for heat transfer measurements
DWO	density wave oscillation
FBCE	Flow Boiling and Condensation Experiment
PCI	parallel channel instability
PDO	pressure drop oscillation

transfer performance while allowing reductions in system weight and volume) due to the likelihood of encountering many different operating environments. Whether utilized in aircraft performing a variety of high-acceleration maneuvers at a range of altitudes, or in spacecraft intended to launch, travel through space, and operate in a distant planetary environment, thermal management systems for these applications will be required to operate across a wide range of thermal conditions and body force fields. Operation across a variety of body force conditions is particularly important for thermal management systems capitalizing on phase change, as the orders of magnitude difference in phase densities can cause these systems to respond strongly to changes in body force [45].

Due to the difficulty of performing system tests under micro-gravity, partial-gravity, and hyper-gravity conditions associated with intended use environments, precise knowledge of how changes in operating conditions affect system performance is imperative to design of phase-change thermal management systems for these applications. In particular, the potential for changes in operating environment to cause instabilities to manifest within the system and adversely affect performance mean a detailed understanding of two-phase flow dynamics and instabilities and their effects on thermal and hydrodynamic characteristics is critical.

### 1.2. Two-phase flow instabilities

Two-phase flow instabilities are commonly described as resulting from interactions between the many thermal and hydraulic phenomenon present in two-phase flows. A significant body of work investigating these phenomena exists, with key instability modes including density wave oscillations (DWOs) [46–50], pressure drop oscillations (PDOs) [51–54], and parallel channel instability (PCI) [55–58]. Much of the work performed is summarized in review articles, including the seminal work of Boure et al. [59]

and more recent reviews of Tadrist [60], Kakac and Bon [61], and Ruspini et al. [62].

The vast majority of work on two-phase flow transient behavior and instabilities concerns only boiling, however, due to the perception that condensation is a more stable process. While this may be true by comparison with boiling, pressure and mass flow rate fluctuations are also commonly seen during flow condensation, meaning it may be that instabilities are present which have not been as thoroughly investigated as those for boiling.

One of the earliest studies including transient flow condensation results was performed by Westendorf and Brown [63] in the mid 1960's, who saw that, for condensation occurring between concurrent flow of saturated vapor and subcooled liquid, high and low frequency oscillatory modes do occur and could be related to subcooling of the liquid phase.

Around the same time, Goodykoontz and Dorsch [64] investigated flow condensation in a more traditional tube-in-tube counterflow configuration. They observed pressure oscillations with frequencies in the 1–10 Hz range, although only for moderate condensation lengths of 1.7–3.7 feet (longer and shorter test sections did not exhibit any fluctuations). Amplitude of oscillation remained below 1 psi in all cases, indicating the oscillations posed no appreciable threat to safe system operation.

Also around this period, Soliman and Berenson [65] performed a detailed investigation of flow condensation in a multi-tube condenser in multiple orientations (vertical upflow, vertical downflow, and horizontal flow) using Freon-113 as working fluid. They observed two distinct oscillatory modes for pressure, one for horizontal and vertical downflow orientations and another for vertical upflow orientation, and correlated amplitude of oscillation for each using experimental data. Also of interest is their observation that amplitude of oscillation is always less than 5% of inlet pressure for vertical downflow and horizontal orientations, and less than 10% of inlet pressure for vertical upflow. This study in particular

was found to be particularly relevant to the present work and is referenced throughout.

Over the ensuing decades, several condensation studies made mention of transient condensation behavior and pressure fluctuations, including flow condensation in a U-tube condenser [66], flow through an annulus [67], multi-tube condensers [68], and micro-channels [42]. Some studies present detailed descriptions, analytic models, and/or computational models including aspects of transient system behavior, ranging from traditional linearized stability models similar to those seen for DWOs and PDOs [69,70] to models attempting to assess the impact of interfacial waves formed by classic hydrodynamic instability present for concurrent flow of two fluids (in this case two phases) [71] on system pressure fluctuations and flow regime transition [42,72,73].

Overall, the available literature dealing with transient aspects of flow condensation is useful in capturing the existence of flow field parameter (e.g., pressure and mass flow rate) oscillations in a majority of test cases, and providing some insight to the physical mechanisms that may be causing them, but lacking a generalized, fundamental approach to analysis which would allow comparison of results across studies and provide means towards achieving a full understanding of the fundamental processes causing oscillations to manifest.

### 1.3. Objectives of study

The present study is part of NASA's Flow Boiling and Condensation Experiment (FBCE), an ongoing collaboration between NASA Glenn Research Center and the Purdue University Boiling and Two-Phase Flow Laboratory (PU-BTPFL) with the goal of developing an experimental facility for the International Space Station (ISS) capable of gathering long term flow boiling and flow condensation data in a microgravity environment. A summary of scientific developments realized as a part of the project can be found in the recent review article prepared by Mudawar [74].

The present study deals with the condensation portion of FBCE and aims to augment prior work dealing with computational prediction of flow condensation [75,76], experimental and analytic assessment of the impact of body force on flow condensation heat transfer coefficient [77,78], and correlation of pressure drop and heat transfer for condensing flows using a large database from available literature [79,80]. This work also serves as a companion piece to a series of recent studies by the present authors investigating transient behavior and instabilities in flow boiling through a single rectangular mini-channel [81–84].

Key goals for the present work are:

- (1) Analysis of transient pressure signals throughout the flow loop to determine potential impact on flow condensation dynamic behavior within the test section.
- (2) Determination of key characteristics of dynamic behavior, including frequency and amplitude of peak oscillatory modes, which may then be evaluated over different ranges of key operating parameters to determine parametric trends.
- (3) Relation of key signal characteristics to physical behavior observed through capture of flow visualization image sequences.

## 2. Experimental methods

Due to the necessary presence of a second fluid acting as coolant against which condensation may take place, design of test modules for flow condensation experience a strong trade between detailed heat transfer measurement and capture of high speed flow visualization images. To overcome this limitation, the present study employs two test sections, one designed specifically for heat

transfer measurements (Condensation Module for Heat Transfer measurements, CM-HT), and one for capture of flow visualization images (Condensation Module for Flow Visualization, CM-FV). These modules are described in detail below.

### 2.1. Condensation module for heat transfer measurements

As its name implies, the CM-HT was designed for the express purpose of gathering detailed flow condensation heat transfer measurements. Fig. 1(a) provides schematics of the module, illustrating its construction as a counterflow heat exchanger created by clamping a stainless-steel tube inside two pieces of polycarbonate with the working fluid, FC-72, condensing along the inner 7.12-mm i.d. tube and cooling water flowing through the outer annulus between the 7.94-mm o.d. tube and the 12.7-mm i.d. channel created by the polycarbonate. Both FC-72 and water flows pass through honeycomb flow straighteners before proceeding through the channel, and short lengths of insulation are present on the outside of the stainless-steel tube near the channel inlet and outlet to allow flow to develop before condensation takes place.

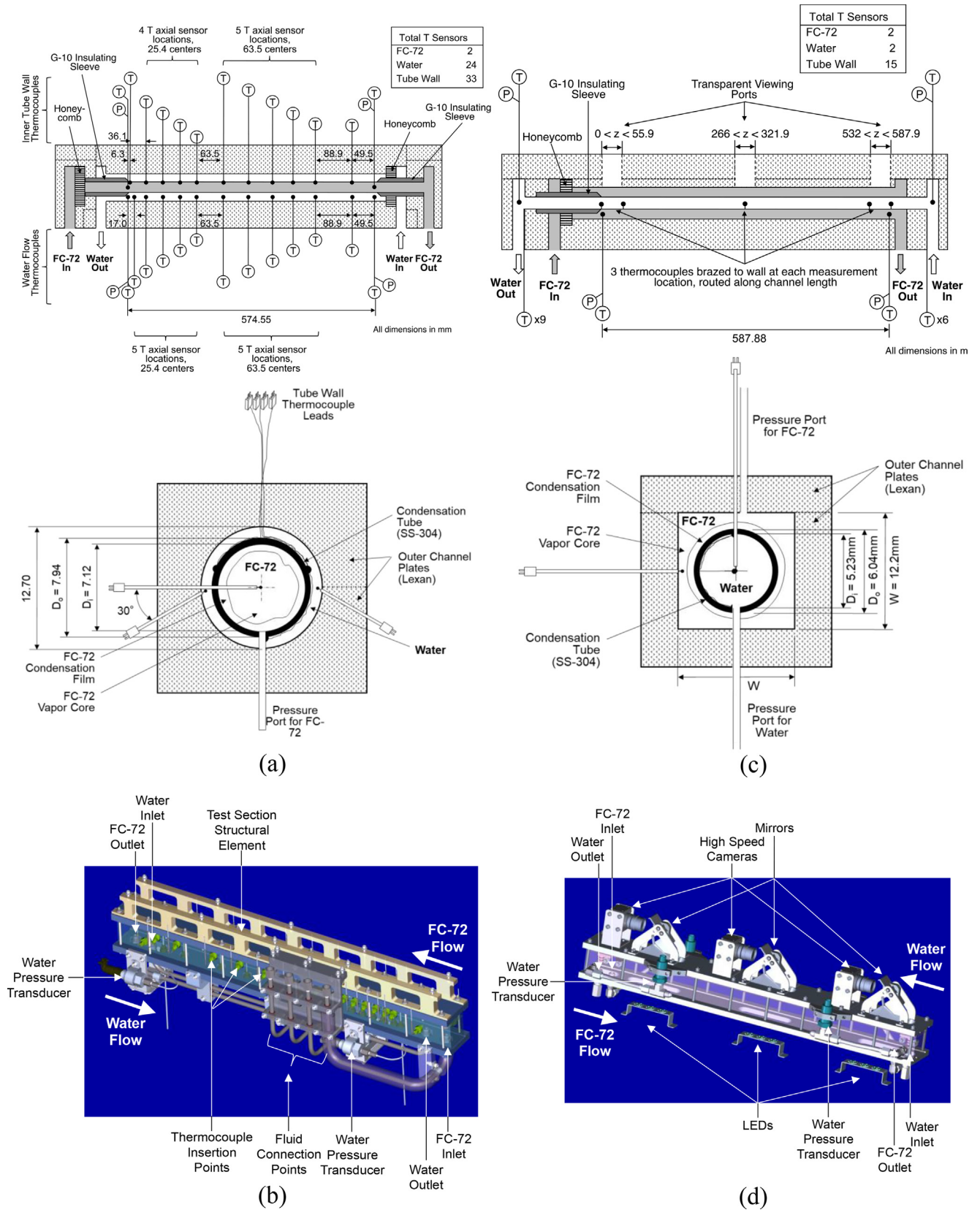
The total condensation length is 574.55 mm, and direct measurement of fluid temperature and pressure is made at the start and end of the length (for both FC-72 and water flows). Both water and tube wall temperatures are made at numerous locations along the channel length, with water measurements made at each axial location by direct immersion in the water flow at two diametrically opposed (180° separation) locations, and tube wall temperatures at each axial location made at three equally spaced (120° separation) locations by thermocouples brazed directly to the tube surface. Measurement locations are concentrated towards the FC-72 inlet to allow detailed information to be gathered in the inlet region (where the condensate film is thin and the condensation heat transfer coefficient changes quickly with axial position), with wider spacing near the FC-72 exit region (where the condensate film is thicker and condensation heat transfer coefficient commonly exhibits less dependence on axial position).

Fig. 1(b) shows a 3-D CAD drawing of the module, prepared for packaging along other modules as part of the FBCE payload intended for use on the ISS. Key points are identified, including water and FC-72 inlet and outlets, thermocouple insertion points, fluid connection points (for interfacing with other modules), and waterside pressure transducers. More so than the schematics presented in Fig. 1(a), the module's construction as a stainless-steel tube suspended between two polycarbonate pieces clamped together by aluminum support plates is clearly apparent here.

### 2.2. Condensation module for flow visualization

Similar to CM-HT, CM-FV is constructed as a counterflow heat exchanger with FC-72 as the working fluid and water acting as coolant. Different from CM-HT, however, is the presence of FC-72 in the annular region, condensing along the outside of the stainless-steel tube through which water now flows as shown in Fig. 1(c). This is done to allow easy optical access to the condensate film as it forms and travels along the outside of the tube.

It should be noted that both stainless-steel tube and polycarbonate channel cross-sectional dimensions have been altered from those in CM-HT, with water now flowing through a 5.23-mm i.d. tube and FC-72 condensing along the same tube's 6.04-mm outer diameter as it flows through the annular region between tube o. d. and the 12.2-mm square polycarbonate channel walls. These differences in dimension from CM-HT are implemented to match hydraulic diameters of the two condensate flow paths, with the hydraulic diameter of the annular region in CM-FV equivalent to that of the 7.12-mm i.d. tube along which FC-72 condenses in CM-HT.



**Fig. 1.** Condensation Module for Heat Transfer measurements (CM-HT) (a) schematics and (b) 3-D drawing, and Condensation Module for Flow Visualization (CM-FV) (c) schematics and (d) 3-D drawing.

As shown in Fig. 1(c), optical access to the condensate film is provided in three locations along the test module, each roughly 55.9-mm in length, with the first beginning at the start of the

587.88-mm condensation length, the second centered on the center of the condensation length, and the third ending at the end of the condensation length.

In order to avoid disturbing FC-72 as it condenses, temperature and pressure measurements of the working fluid are limited to inlet and outlet locations. On the water side, however, in addition to inlet and outlet temperature and pressure measurements made by direct immersion, wall temperatures are also recorded at five axial positions within the stainless-steel tube. These positions correspond to just upstream and downstream of the first and third imaging location as well as the center of the second imaging location. Each axial measurement location has three measurement points: two brazed to the inner tube wall separated by 180° and one exposed to water flow at the tube centerline. Thermocouple wires are routed along the channel to the nearest exit (inlet or outlet) where they are removed from the flow through appropriate fittings.

Similar to Fig. 1(b), Fig. 1(d) shows a 3-D CAD drawing of CM-FV with key features identified. Of particular note in this subfigure are the three sets of LEDs used to provide backlighting for images, as well as the use of mirrors to direct the field of view of each camera towards the condensate film.

High speed images captured during CM-FV tests are performed at two speeds (depending on flow rate of condensate): 2000 frames per second (fps) with pixel resolution of 2040 × 174, and 4000 fps with pixel resolution of 2040 × 81.

2.3. Experimental facility

The experimental facility used for the present tests was developed as part of NASA's ongoing FBCE and intended to serve as a brass-board system useful for testing of flight hardware prototypes. Fig. 2(a) and (b) provide schematics and images of the facility, respectively, with key components labeled.

Fig. 2(a) shows the working fluid, dielectric FC-72, is circulated within the primary loop by use of a magnetically coupled Micropump gear pump. Flow first passes through a 5-μm filter to remove any particulates entrained, then progresses through a Coriolis flow meter used to measure mass flow rate. Exiting the flow meter the

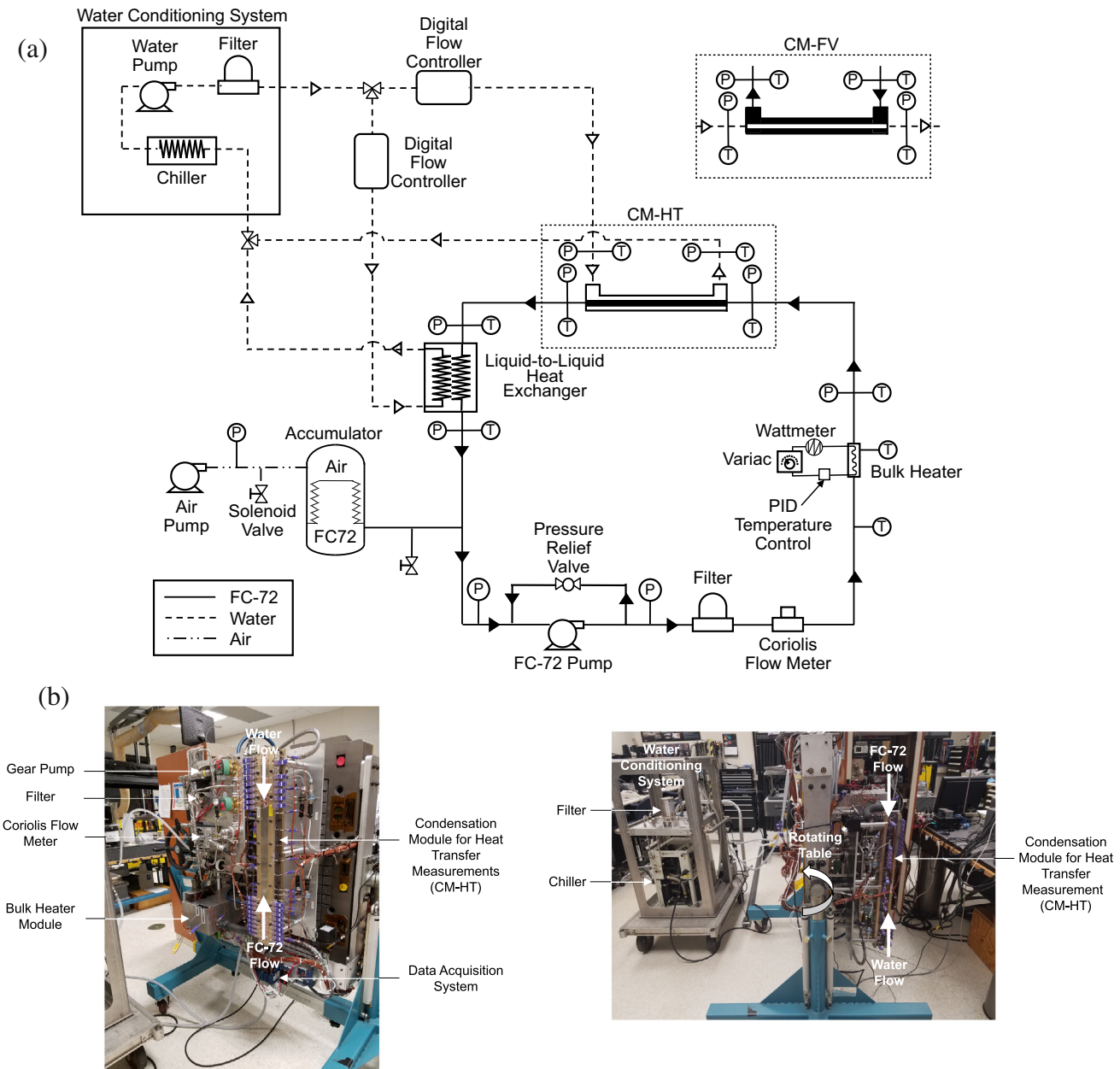


Fig. 2. (a) Schematic of flow loop used in current study, and (b) photos of facility with key components identified.

fluid enters the bulk heater, used to set thermodynamic state at the inlet of the test section.

The bulk heater used in the current experiments is configured to reflect the manner in which it will be utilized in the final ISS experiments. Two modes of operation are possible, one with PID control of bulk heater metal temperature and one with constant power provided to the bulk heater. Cases with two-phase (saturated mixture) inlet conditions are run in constant power mode to allow calculation of thermodynamic quality at the bulk heater outlet without the need to integrate a power curve in time (necessary for cases with PID temperature control). Cases with superheated inlet conditions are run in temperature control mode, with power supplied to the bulk heater varied to maintain a set-point temperature measured within the bulk heater wall.

Continuing past the bulk heater, the working fluid passes through a short insulated length and enters the test section. As mentioned when discussing each respective module in the preceding sections, flow through the test section is condensed by use of cooling water supplied in counterflow configuration. Fig. 2(a) illustrates cooling water is conditioned and supplied through use of a secondary loop containing a water conditioning system and multiple digital flow controllers. Water flow for both the test section and secondary condenser (used to ensure FC-72 is returned to a sub-cooled, single phase liquid state prior to returning to the pump) is supplied by a water conditioning unit, which includes a Merlin M33 chiller, pump, and filter. Both flow controllers are computer controlled and allow precise control of water flow rates through both the test section and the secondary condenser.

Upon exiting the test section, the fluid enters the secondary condenser. This unit is a custom built, liquid-to-liquid, helical tube-in-tube heat exchanger operated in counterflow configuration, and represents a prototype for the condenser to be used during ISS experiments. Exiting the condenser, the fluid passes an accumulator (used to accommodate volume changes within the loop due to phase change) prior to returning to the pump.

Similar to the condenser, the accumulator is a custom build prototype of the unit to be used during ISS experiments. Important to note is the presence of a small pump and solenoid valve on the air side of the accumulator, allowing active system pressure adjustment during experiments and evaluation of parametric trends relating to changes in system pressure during data analysis.

It should be noted that all primary loop hardware (including accumulator airside components) are mounted on a rotating bench-top, shown in Fig. 2(b). This, coupled with the connection of water lines through flexible tubing, allows for easy transition between operating orientations during testing.

#### 2.4. Operating conditions, operating procedure, and measurement uncertainty

Operating conditions for the current set of tests are selected to match those outlined in NASA's Science Requirements Document for FBCE, intended to allow for characterization of key hardware under relevant operating conditions as well as generation of a database of 1-g results which may be compared to microgravity data. Table 1 outlines target operating conditions for the current set of experiments, where, for each FC-72 mass velocity, every combination of water mass velocity, operating pressure, and inlet quality is tested. Additionally, every combination of operating conditions is tested in vertical upflow, vertical downflow, and horizontal flow orientations, allowing investigation of body force effects on flow behavior. Overall, tests conducted across all three orientations include 57 cases in vertical upflow, 57 cases in vertical downflow, and 69 cases in horizontal flow, for a total of 183 data points, encompassing mass velocities of  $G_{FC} = 40.0\text{--}362.1 \text{ kg/m}^2 \text{ s}$  and  $G_{H_2O} = 64.6\text{--}388.8 \text{ kg/m}^2 \text{ s}$ , module FC-72 inlet pressure

**Table 1**  
Target operating conditions for current study.

$G_{FC}$ [kg/m <sup>2</sup> s]	$G_{H_2O}$ [kg/m <sup>2</sup> s]	$P_{FC,in}$ [kPa]	$x_{e,in}$
50	130, 260, 390	130, 160	1.0
100	130, 260, 390	130, 160	1.0
100	390	130	0.4, 0.6, 0.8
150	130, 260, 390	130, 160	1.0
150	390	160	0.4, 0.6, 0.8
200	130, 260, 390	130, 160	1.0
200	390	130, 160	0.4, 0.6, 0.8
250	130, 260, 390	130, 160	1.0
300	130, 260, 390	130, 160	1.0
300	390	130, 160	0.4, 0.6, 0.8
325	130, 260, 390	130, 160	1.0
350	390	130, 160	0.4, 0.6, 0.8

$P_{in} = 126.3\text{--}164.3 \text{ kPa}$ , bulk heater power  $Pwr_{BH} = 199.7\text{--}1578.0 \text{ W}$ , inlet quality  $x_{e,in} = 0.01\text{--}1.22$ , and exit quality  $x_{e,out} = -0.78$  to  $0.47$ . It should be noted here that values of inlet and exit quality greater than 1.0 and less than 0 refer to superheated and subcooled conditions, respectively. They are calculated for FC-72 according to the expressions

$$x_{e,in} = \frac{Pwr_{BH} - \dot{m}_{FC} c_{p,f,FC} (T_{FC,sat} - T_{BH,in})}{\dot{m}_{FC} h_{fg,FC}}, \quad (1)$$

and

$$x_{e,out} = \frac{Pwr_{BH} - \dot{m}_{FC} c_{p,f,FC} (T_{FC,sat} - T_{BH,in}) - \dot{m}_{H_2O} c_{p,f,H_2O} (T_{H_2O,out} - T_{H_2O,in})}{\dot{m}_{FC} h_{fg,FC}}, \quad (2)$$

where  $Pwr_{BH}$ ,  $\dot{m}$ ,  $c_p$ , and  $h_{fg}$  are, respectively, the power supplied to FC-72 by the bulk heater, fluid mass flow rate, liquid specific heat, and enthalpy of vaporization. All fluid properties for each phase are evaluated at local pressures.

It should be noted here that for cases with superheated inlet conditions, inlet quality is calculated directly based on measured temperature and pressure at the module inlet. For cases with saturated mixture inlet conditions, Eq. (1) is evaluated after adjusting power supplied by the bulk heater  $Pwr_{BH}$  to account for heat loss.

Tests are conducted by setting FC-72 flow rate, water flow rate, and bulk heater power to levels necessary to achieve the desired flow rates and inlet quality in the test section. Pressure at the test section inlet is adjusted using the pump and valve on the air-side of the accumulator. Multiple minor adjustments to all parameters are necessary, as changes to any one parameter would alter others. Once desired test conditions are reached, the system is allowed to sit for 3–5 min to ensure conditions are steady and no slow transients are present which may affect interpretation of results. After confirming the system is steady, data are collected for an additional period of five minutes: three minutes at a sampling rate of 5 Hz, and two minutes at 200 Hz (with sampling rate changed via a command in the LabView program controlling data acquisition). After completing data collection, tests move to the next desired set of operating conditions. The present study only presents results sampled at 200 Hz, done to allow analysis of frequency composition up to 100 Hz (determined by the Nyquist sampling criterion).

Data collection for all temperature, pressure, flow rate, and power measurements is handled by a cDAQ-9178 data acquisition system with one NI-9205 analog input module and four NI-9214 thermocouple modules, all controlled by LabView. All temperature measurements are made with type-T thermocouples having uncertainty of  $\pm 0.4 \text{ }^\circ\text{C}$ , and pressure measurements using STS absolute pressure transducers with an accuracy of  $\pm 0.1\%$ . Flow rates (and thus mass velocities) are measured using Bronkhorst Cori-Flow Coriolis flow meters with an accuracy of  $\pm 0.2\%$ , and bulk heater power input is calculated from voltage and current data with an

accuracy of  $\pm 0.2$  W. All properties are evaluated at local pressure using data obtained from NIST.

### 3. Transient pressure results and existence of key oscillatory modes

As mentioned in Section 1, literature investigating transient aspects of flow boiling is more prolific than that for flow condensation, leaving significant questions regarding formation and characteristics of instabilities and oscillations in condensing systems. Towards this end, the present work will begin with investigation of the presence of oscillatory modes within condensing flows.

#### 3.1. Observation of oscillatory modes within CM-HT

Fig. 3(a)–(c) present CM-HT inlet and outlet pressure results plotted over a 20-s period, a shortened 3-s window (to better highlight curve characteristics), and associated fast Fourier transform results (with transform performed over the 20-s period) in vertical upflow, vertical downflow, and horizontal flow orientations, respectively. Each plot corresponds to similar superheated FC-72 inlet conditions with FC-72 mass velocity  $G_{FC} \sim 300$  kg/m<sup>2</sup> s, cooling water mass velocity  $G_{H2O} \sim 129$  kg/m<sup>2</sup> s, FC-72 module inlet pressure  $P_{in,ave} \sim 130$  kPa, FC-72 module inlet quality  $x_{e,in} \sim 1.05$ , and exit quality  $x_{e,out} \sim 0.45$ .

Immediately apparent when comparing subfigures is the range of oscillatory behavior exhibited for each case. Fig. 3(a) shows vertical upflow condensation experiencing almost no oscillations (evident from both transient plots and the lack of peaks in FFT results). Meanwhile, vertical downflow, Fig. 3(b), and horizontal flow, Fig. 3(c), clearly show the presence of oscillatory modes in their respective frequency response plots, with most oscillatory behavior observed in the 1–10 Hz frequency range.

Fig. 4(a)–(c) show similar results, this time for saturated rather than superheated FC-72 inlet conditions, with  $G_{FC} \sim 200$  kg/m<sup>2</sup> s,  $G_{H2O} \sim 388$  kg/m<sup>2</sup> s,  $P_{in,ave} \sim 130$  kPa,  $x_{e,in} \sim 0.15$ , and  $x_{e,out} \sim -0.25$ . Results for vertical upflow, Fig. 4(a), now exhibit large amplitude oscillations, with successively lower amplitude oscillatory behavior observed for vertical downflow, Fig. 4(b), and horizontal flow, Fig. 4(c). Oscillations present in the vertical upflow are concentrated around 10 Hz, while those in vertical downflow and horizontal flow are present primarily near 1 Hz, with secondary peaks present near 10 Hz.

Figs. 3(a)–(c) and 4(a)–(c) combine to illustrate two key points. First, well defined oscillatory modes are present within flow condensation for certain operating conditions, and second, these oscillatory modes (and even the existence of these modes) vary depending on operating conditions. Prior to undertaking parametric analysis to better characterize these phenomena, however, it is necessary to determine whether these oscillations are physical in nature (arising from inherent aspects of two-phase flow and/or condensation), or a manifestation of mechanically induced behavior propagated from another point within the flow loop.

Towards this end, Fig. 5(a)–(d) provide transient plots and frequency response curves for pump inlet and outlet pressures, bulk heater power input, CM-HT water inlet and outlet pressures, and CM-HT FC-72 inlet and outlet pressures, respectively. The case shown here corresponds to vertical upflow with  $G_{FC} = 206.1$  kg/m<sup>2</sup> s,  $G_{H2O} = 388.1$  kg/m<sup>2</sup> s,  $P_{in,ave} = 129.1$  kPa,  $x_{e,in} = 1.27$ , and  $x_{e,out} = 0.15$ . The goal of these plots is to characterize oscillatory behavior induced by key active mechanical components within the loop, and compare it to that observed within the region of interest (FC-72 flow through CM-HT) to determine if oscillatory behavior within the test section is impacted by mechanical components within the loop. This is similar to analysis performed at length for flow boiling in a prior work [82].

Fig. 5(a) shows clear presence of significant oscillations for both pump inlet (suction-side) and outlet pressures, with difficulty distinguishing between the two due to small magnitude pressure change across the pump and high oscillatory amplitude for each signal. Performing FFT's on each signal reveals the majority of oscillatory modes are found in the high-frequency range (20–100 Hz), with clear dominant peaks for both inlet and outlet pressure signals at  $\sim 90$  Hz. The fact these modes are very sharp is indicative of mechanical, pump-induced oscillatory behavior [81].

Fig. 5(b) illustrates the square-wave nature of power input through the bulk heater while the system operates in constant-temperature mode (with a PID controller pulsing power input to achieve a desired bulk heater temperature). This mode of operation is only used for a subset operating conditions tested (those for which superheated inlet conditions are desired), but, due to its oscillatory nature, it is reasonable to speculate on whether flow dynamic behavior is impacted. The frequency response plot shown in Fig. 5(b) indicates peak frequencies are present in the low-frequency range of the spectrum (0.1–1 Hz), with clear peaks decreasing in amplitude as frequency increases. This is expected based on the known decomposition of square waves [85].

Fig. 5(c) provides plots of CM-HT waterside inlet and outlet pressures. Although the water conditioning loop is separate from the primary (FC-72) flow loop, presence of strong oscillatory modes within the water loop could potentially cause vibrations within the test module that could be picked up within the FC-72 pressure signal. This is not the case for the current setup, however, as Fig. 5(c) clearly shows near-zero oscillatory behavior present within the waterside of the system.

Finally, Fig. 5(d) provides transient and associated frequency composition plots of FC-72 pressure at the inlet and outlet of CM-HT, with difficulty distinguishing between the two again due to small magnitude change and relatively high amplitude oscillations. These plots show presence of a low-amplitude oscillatory mode over a narrow frequency band centered on  $\sim 10$  Hz. This is clearly different from oscillatory modes observed at other locations throughout the loop, indicating oscillatory behavior observed within the FC-72 side of the test section may be considered independent of other oscillatory modes introduced in the system.

This conclusion is reinforced by the fact that dominant oscillatory modes are only observed within the test section for certain combinations of operating conditions, while behavior across the pump, bulk heater, and water loop remains largely constant regardless of operating conditions. The dependence of existence of peak oscillatory modes within the test section on operating conditions is discussed further in the following subsection.

#### 3.2. Existence of peak oscillatory mode within CM-HT

In order to evaluate parametric trends regarding the presence of a clearly defined peak oscillatory mode within the test section, it is first necessary to set criteria determining whether a peak oscillatory mode is in fact present. Then, once a peak oscillatory mode has been identified, some measure of its intensity should be provided for comparison with oscillatory modes present under other operating conditions.

Fig. 6(a)–(c) depict the process by which these two key pieces of information are determined for three sets of operating conditions, all in vertical upflow. First, fast Fourier transforms are performed on test module FC-72 inlet and outlet pressure signals to determine frequency composition of any oscillations present (only results corresponding to inlet pressure signals are shown in the present plot). Frequency response curves are then passed through a 10 Hz low-pass filter to help smoothen results and provide a continuous response curve. The low-pass filter used is a second-order Butterworth digital filter with transfer function

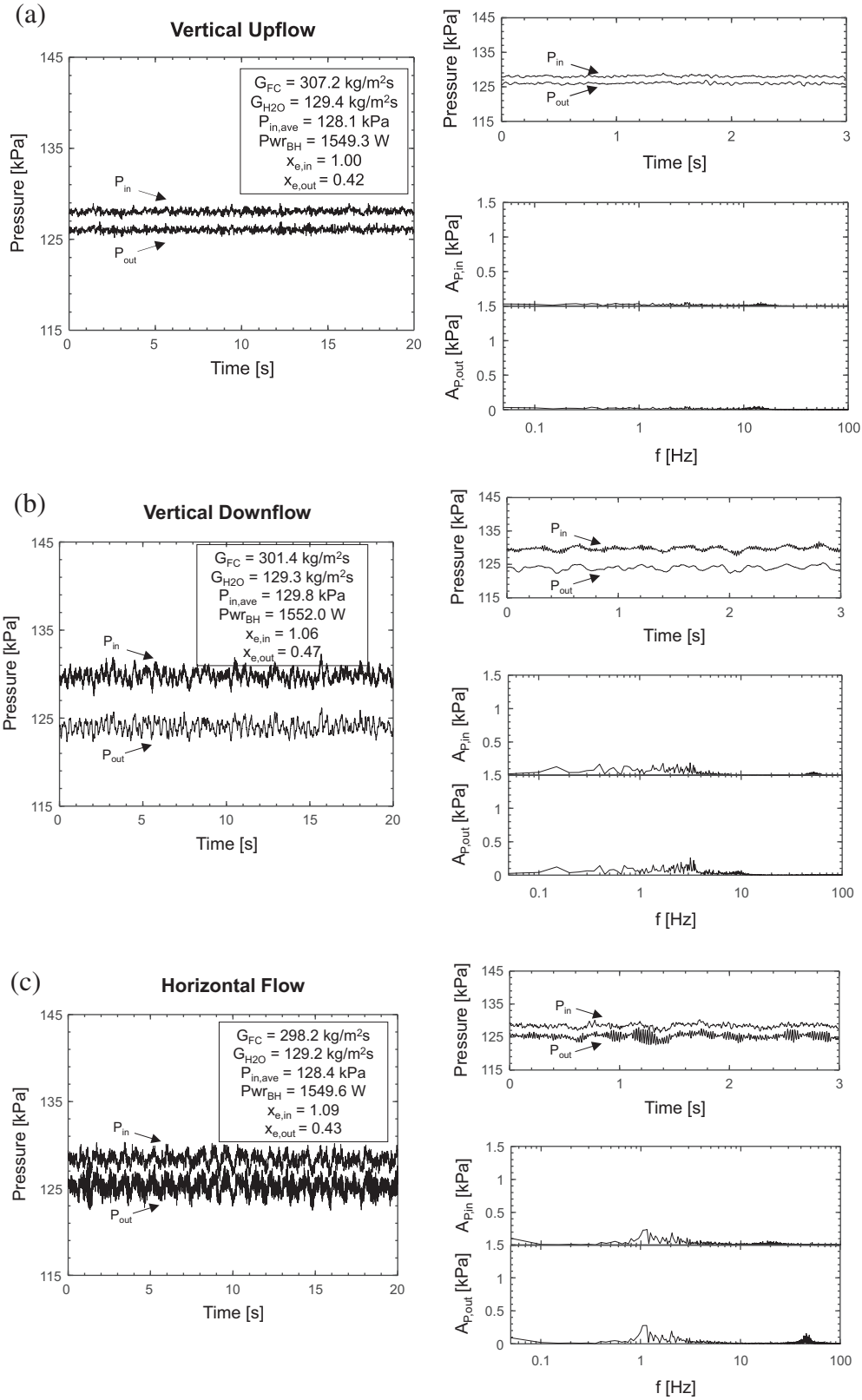


**Fig. 3.** Transient CM-HT inlet and outlet pressure curves over 20-s and 3-s periods, along with associated fast Fourier transforms taken over the 20-s period for (a) vertical upflow, (b) vertical downflow, and (c) horizontal flow orientations with superheated vapor inlet.

$$H(z) = \frac{0.02 + 0.04z^{-1} + 0.02z^{-2}}{1.0 - 1.56z^{-1} + 0.64z^{-2}}, \quad (3)$$

where  $z$  is the digital domain variable. Coefficients shown here are truncated for presentation but preserved with additional significant figures by the python script used to generate them [86].

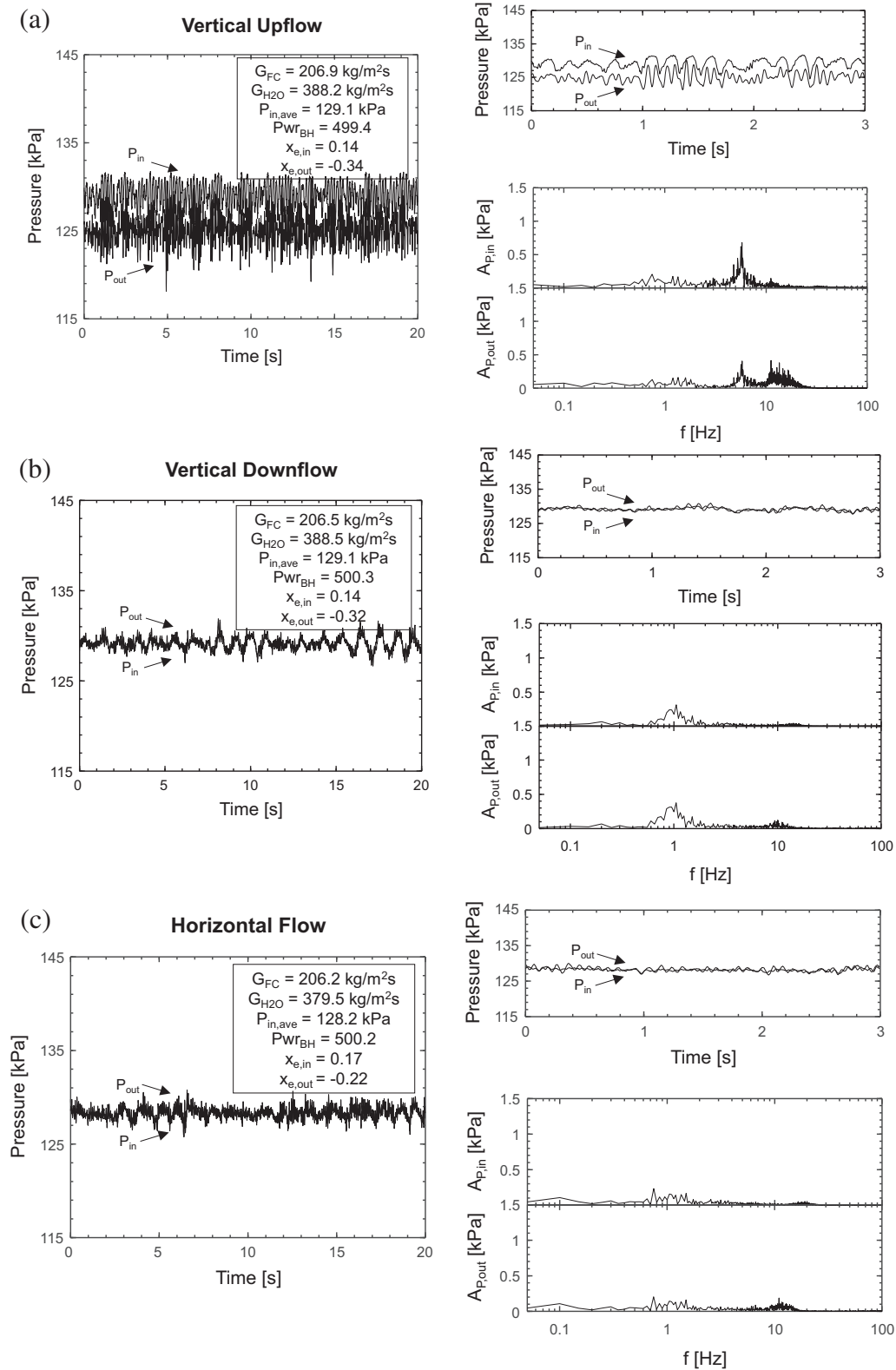


**Fig. 4.** Transient CM-HT inlet and outlet pressure curves over 20-s and 3-s periods along with associated fast Fourier transforms taken over the 20-s period for (a) vertical upflow, (b) vertical downflow, and (c) horizontal flow orientations with saturated mixture inlet.

The low pass filter applied here is intended to allow for determination of the  $Q$  Factor (or  $Q$ , for short) of peaks present in the frequency response of each signal. Prior to this calculation, however, it is necessary to determine if any peaks are present within the frequency response. This is done by checking whether the maximum value of the frequency response satisfies two conditions:

- (1) The difference between the maximum and mean amplitude values on the frequency response plot is greater than 0.1,

$$\Delta A_{max,mean} = \max(A_p) - \text{mean}(A_p) > 0.1. \quad (4)$$

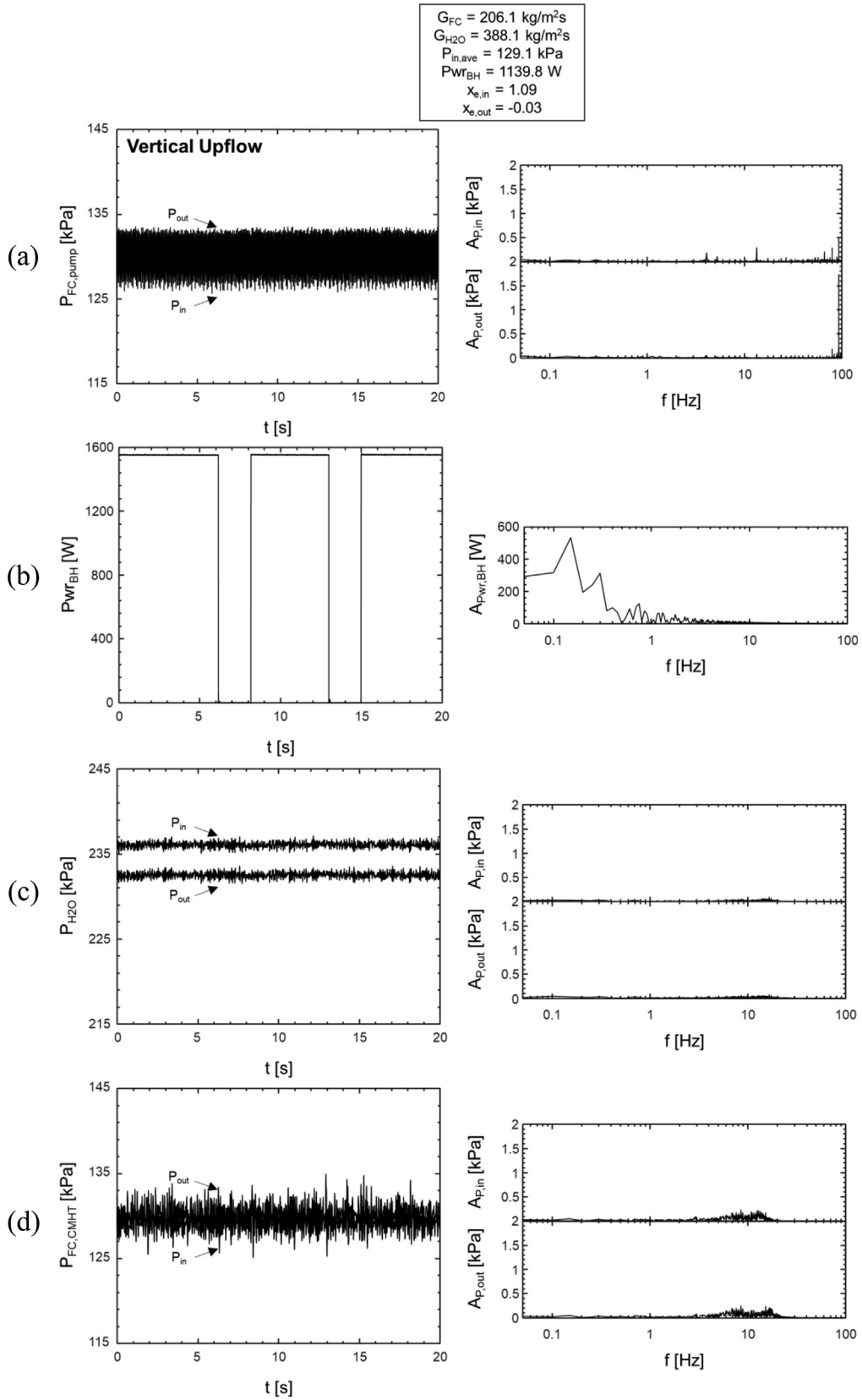


**Fig. 5.** Sample transient plots and associated fast Fourier transforms for (a) FC-72 pump inlet and outlet pressures, (b) bulk heater power input, (c) CM-HT water inlet and outlet pressures, and (d) CM-HT FC-72 inlet and outlet pressures.

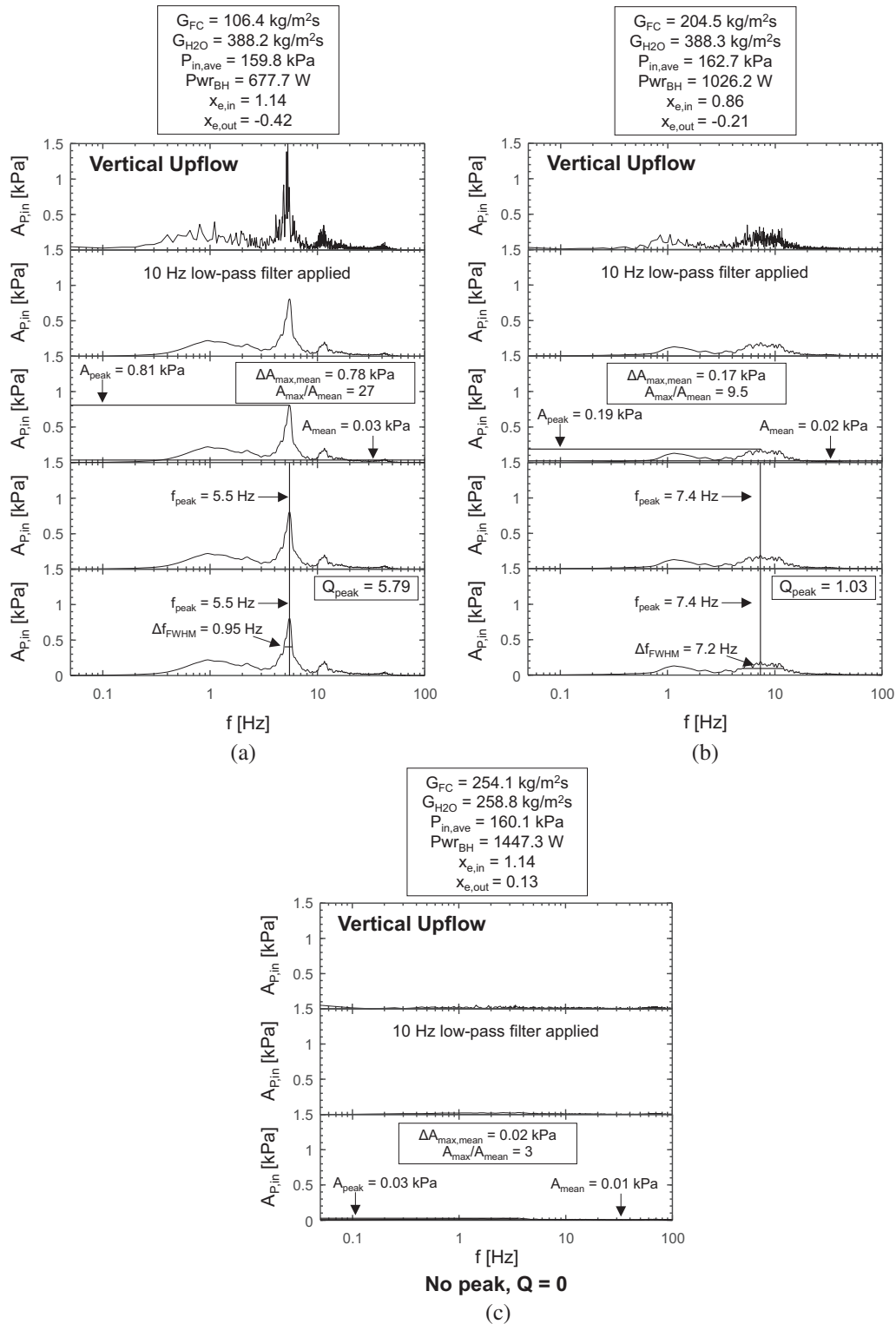


**Fig. 6.** Process of determining Q Factor for peak frequency of oscillation by taking fast Fourier transform of 20-s duration inlet pressure signal, applying 10-Hz low pass filter to FFT curve, determining if a true peak exists, identifying the frequency associated with the peak, and determining the associated Q Factor for cases with (a) high Q, (b) moderate Q, and (c) no peak.

(2) The ratio of maximum to mean amplitude values is greater than 2,

$$A_{max}/A_{mean} = \frac{\max(A_p)}{\text{mean}(A_p)} > 2. \quad (5)$$

This set of criteria determines (1) that the max value of the frequency response is sufficiently greater than the mean value (with the value here determined by inspection of the entire dataset), and (2) that the ratio of max value to mean value is sufficiently high,

so the satisfaction of both criteria ensures the presence of a true peak in the frequency response.

It should be noted that the second criterion listed above is not used to exclude any cases in the present dataset, but may be important for application to other datasets where significant variations in noise (possibly due to mechanical vibrations from outside sources [87]) are present.

Once it has been determined whether a true peak exists in the frequency response curve (e.g., Fig. 6(a) and (b), but not Fig. 6(c)), the sharpness of the peak may be determined by calculating its Q Factor. This is done by determining the frequency at which the peak occurs and dividing it by the full width half maximum (amplitude) frequency range, or

$$Q = \frac{f_{A=\max(A)}}{\Delta f_{A=1/2 \max(A)}} = \frac{f_{\text{peak}}}{\Delta f_{\text{FWHM}}}, \quad (6)$$

In physical terms, Q Factor represents the concentration of oscillatory energy about a single frequency value. Fig. 6(a) exhibits a very sharp peak at 5.5 Hz, and the associated Q Factor of 5.79 indicates

that the energy associated with this oscillatory mode is concentrated in a narrow band about that peak. Fig. 6(b), meanwhile, exhibits a dominant oscillatory mode that is distributed over a wide frequency range, reflected in a Q Factor of 1.03. Fig. 6(c) exhibits no clear peak in its frequency response plot, and is assigned a Q Factor of 0 (indicating an approximately flat frequency response and the nonexistence of a dominant oscillatory mode).

It should be noted that all values of Q presented hereafter are calculated for both inlet and outlet FC-72 pressure signals then averaged, providing a single Q value for each set of operating conditions.

Having presented a methodology by which the existence of a dominant oscillatory mode may be determined and its intensity characterized, it is possible to undertake a parametric evaluation of the influence of different key operating conditions on formation of dominant oscillatory modes. Fig. 7(a)–(c) present plots of Q Factor versus FC-72 mass velocity, inlet quality, exit quality, and (time-averaged) inlet pressure for vertical upflow, vertical downflow, and horizontal flow orientations, respectively.

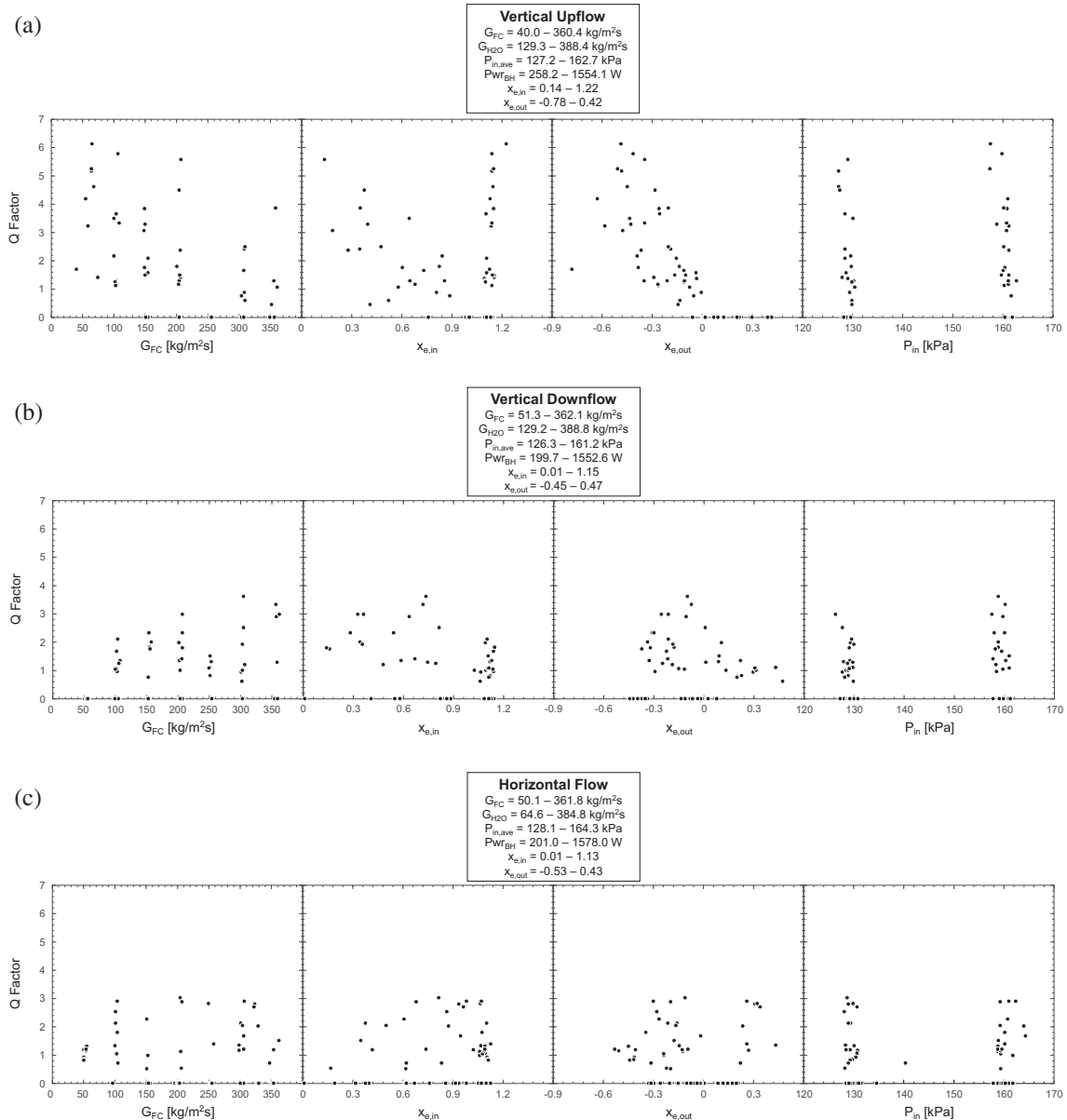


Fig. 7. Plots of Q Factor versus FC-72 mass velocity, inlet quality, exit quality, and inlet pressure, for all cases in (a) vertical upflow, (b) vertical downflow, and (c) horizontal flow orientations.

Fig. 7(a) shows  $Q$  Factor decreasing as both mass velocity and exit quality are increased. These trends indicate vertical upflow condensation exhibits less pronounced oscillatory behavior (meaning a clearly defined oscillatory mode is not present) as mass velocity is increased and as liquid content at the exit of the channel is reduced. This makes intuitive sense, as body force acts to destabilize the liquid film in vertical upflow orientation, with increased mass velocity (increased liquid inertia and interfacial shear) as well as reduced liquid content acting to reduce the influence of body force on hydrodynamic behavior. No discernible trends are present for variations in inlet quality and inlet pressure.

Fig. 7(b) shows similar plots for results obtained in vertical downflow orientation. Counter to that seen for vertical upflow, results here indicate increased oscillatory behavior as mass velocity is increased in vertical downflow orientation. Similar to vertical upflow, values of  $Q$  Factor also decrease for increases in channel exit quality, despite the fact the majority of downflow cases with no peak oscillatory mode ( $Q = 0$ ) occur for cases with negative exit quality. Similar to vertical upflow, little or no trends are present for variations in inlet quality and operating pressure.

Fig. 7(c), presenting results obtained during horizontal flow condensation, exhibits no appreciable trend in values of  $Q$  for changes in mass velocity, inlet quality, exit quality, or operating pressure.

Analyzing trends across all subfigures in Fig. 7, body force has a significant effect on the manifestation of oscillatory behavior in flow condensation, and one which is compounded by changes to key operating parameters. To better understand physical phenomena influencing dynamic behavior,  $Q$  Factor will be plotted versus several relevant dimensionless groups. These include inlet vapor Reynolds number,  $Re_{g,in}$ , defined as

$$Re_{g,in} = \frac{G_{FC} x_{e,in} D_h}{\mu_g}, \quad (7)$$

where  $D_h$  is the channel hydraulic diameter and  $\mu_g$  the dynamic viscosity of vapor, inlet vapor Weber number,  $We_{g,in}$ , defined as

$$We_{g,in} = \frac{\rho_g (G_{FC} x_{e,in} v_g)^2 D_h}{\sigma}, \quad (8)$$

where  $\rho_g$  is vapor density,  $v_g$  vapor specific volume, and  $\sigma$  surface tension, and inlet vapor Froude number,  $Fr_{g,in}$ , defined as

$$Fr_{g,in} = \frac{v_g G_{FC} x_{e,in}}{\sqrt{g D_h}}, \quad (9)$$

where  $g$  is Earth's gravitational constant. Similar values are also defined in terms of channel exit and liquid properties, defined as

$$Re_{f,out} = \frac{G_{FC} (1 - x_{e,out}) D_h}{\mu_f}, \quad (10)$$

$$We_{f,out} = \frac{\rho_f (G_{FC} (1 - x_{e,out}) v_f)^2 D_h}{\sigma}, \quad (11)$$

and

$$Fr_{f,out} = \frac{v_f G_{FC} (1 - x_{e,out})}{\sqrt{g D_h}}, \quad (12)$$

for exit liquid Reynolds number, Weber number, and Froude number, respectively. It should be noted that properties used in the calculation of all dimensionless groups are evaluated at time-averaged inlet pressure for each case and the value of  $g$  remained constant for all orientations (no sign changes).

Similar to Fig. 7(a)–(c), Fig. 8(a)–(c) provide plots of  $Q$  versus each of the dimensionless groups presented in Eqs. (7)–(12) for vertical upflow, vertical downflow, and horizontal flow orientations, respectively. Fig. 8(a) shows quadratic decreases in

$Q$  for changes in dimensionless groups based on inlet parameters, while those based on outlet parameters exhibit linear decreases. The general decreasing trend is consistent with that seen for mass velocity in Fig. 7(a), as mass velocity is present in the numerator of every dimensionless group here. The difference in slope between dimensionless groups based on inlet and outlet parameters, however, indicates the intensity of oscillatory modes in vertical upflow condensation is more strongly tied to inlet conditions than exit.

Fig. 8(b) provides similar plots for vertical downflow. Dimensionless groups based on inlet parameters exhibit no clear trends, while those based on exit parameters show linear increases in  $Q$  as Reynolds, Weber, and Froude numbers are increased.

Fig. 8(c) indicates results for the horizontal orientation again exhibit no appreciable trends for any of the parameters evaluated here. It is worth noting, however, that tests conducted in horizontal orientation exhibit the lowest  $Q$  values as well as the highest percentage of  $Q = 0$  cases (46% versus 39% for vertical downflow and 28% for vertical upflow), indicating it is the most stable orientation. Vertical upflow, meanwhile, can be seen to exhibit the highest  $Q$  values of the three orientations, with vertical downflow falling between the two.

Overall, Figs. 7(a)–(c) and 8(a)–(c) indicate that, for vertical upflow and downflow orientations, mass velocity is the key parameter governing existence of a dominant oscillatory mode. In vertical upflow increases in mass velocity exhibit a stabilizing effect on the flow, while in vertical downflow increases in mass velocity destabilize the flow. Further, trends regarding  $Q$  Factor (interpreted here as a measure of the intensity of a dominant oscillatory mode) depend strongly on channel inlet and vapor parameters for vertical upflow and channel exit and liquid parameters for vertical downflow. This is a key outcome, as it implies different physical processes govern flow dynamics in vertical upflow and downflow orientations.

$Q$  Factor alone is insufficient to fully characterize flow dynamic behavior, however, as it does not include information regarding differences in amplitude and frequency of oscillations. Thus, moving forward, only cases with non-zero  $Q$  will be considered, and amplitude and frequency at which they exhibit peak oscillations will be analyzed.

#### 4. Characterization of dominant oscillatory mode

Prior to analyzing trends regarding amplitude and frequency of peak oscillatory modes, it is first necessary to discuss detection of peak frequency and amplitude of oscillation. Fig. 9(a) and (b) present the process used step-by-step. Fig. 9(a) provides plots of CM-HT inlet and outlet pressure measurements for a case in vertical upflow with  $G_{FC} = 106.4 \text{ kg/m}^2 \text{ s}$ ,  $G_{H_2O} = 388.2 \text{ kg/m}^2 \text{ s}$ ,  $P_{in,ave} = 159.8 \text{ kPa}$ ,  $x_{e,in} = 1.14$ , and  $x_{e,out} = -0.42$ . Fig. 9(b) shows associated fast Fourier transform results (frequency response plots) for each signal, again calculated over the 20-s period as indicated in previous sections.

Frequency response plots in Fig. 9(b) have peak frequency (frequency value associated with maximum amplitude on the response plot) labeled, as well as a vertical dashed line drawn at 30 Hz. This is done to indicate filter cutoff frequency used to filter transient pressure curves prior to amplitude detection as shown in Fig. 9(c), applied to fluctuating pressure signals (zero mean) defined as

$$P' = P - P_{ave}, \quad (13)$$

where  $P'$  is the fluctuating component of pressure,  $P$  is instantaneous pressure, and  $P_{ave}$  is average pressure over the 20-s period under evaluation.

The concept behind application of a low pass filter (applied as a second order Butterworth filter function, similar to that provided

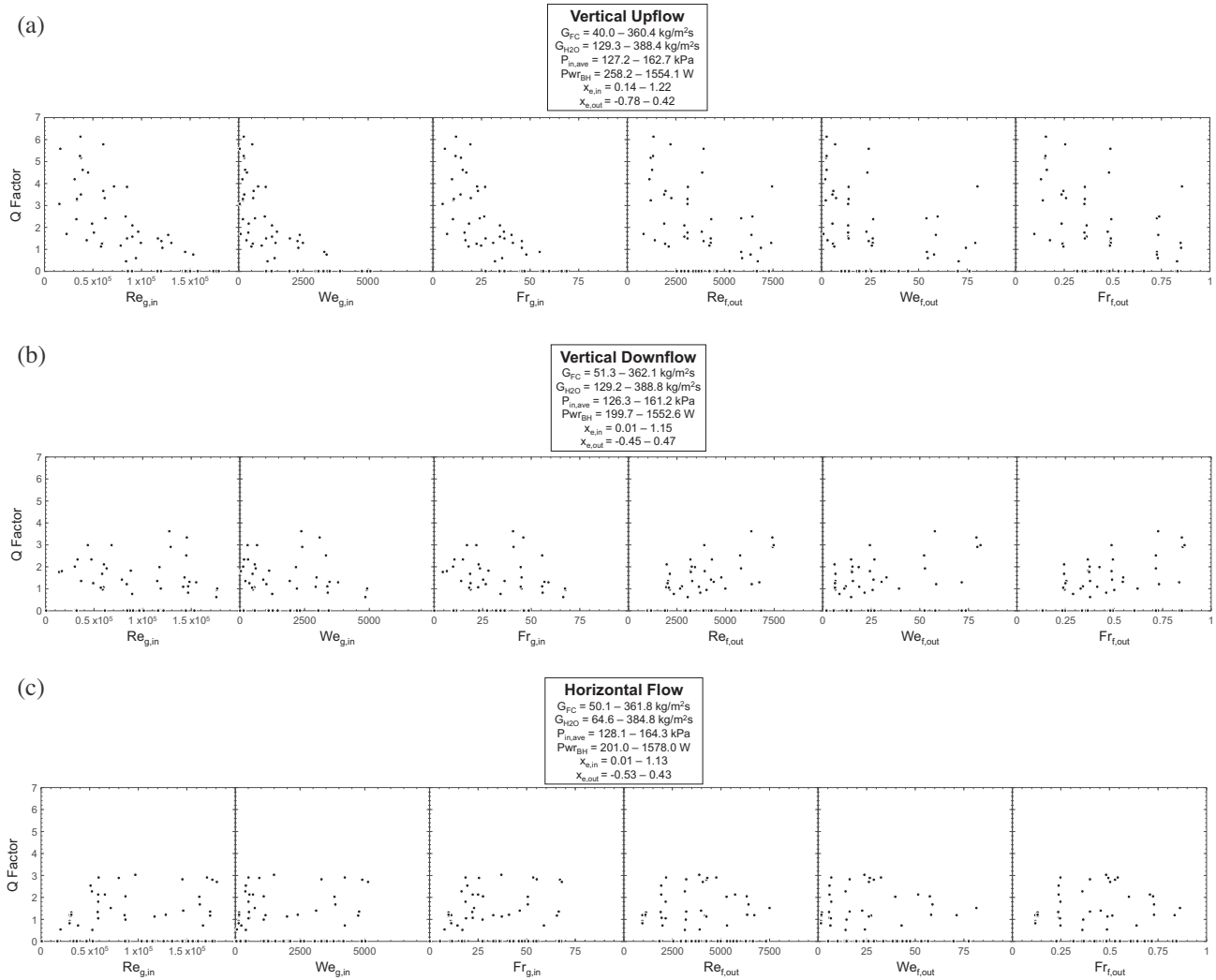


**Fig. 8.** Plots of Q Factor versus FC-72 inlet vapor Reynolds, Weber, and Froude numbers, and exit liquid Reynolds, Weber, and Froude numbers, for all cases in (a) vertical upflow, (b) vertical downflow, and (c) horizontal flow orientations.

in Eq. (3) although with different filter coefficients placing cutoff frequency at 30 Hz) is isolation of the oscillatory amplitude attributable to relevant physical (peak) oscillatory mode and elimination of any high-frequency sources which may be present. It is necessary to place filter cutoff frequency at such a high value due to the necessity of capturing peak frequencies for certain combinations of operating conditions which yield them at relatively high frequencies ( $\sim 20$  Hz), something which will be discussed in subsequent sections.

After filtering transient pressure signals, Fig. 9(d) provides an example of detection of oscillatory amplitude, defined as half the maximum pressure value minus the minimum pressure value evaluated over the same 20-s period on which fast Fourier transforms are performed and shown in Fig. 9(a) (Fig. 9(c) and (d) only include 3 s of transient data to better highlight curve characteristics). It is important to note here that all cases evaluated in the current study correspond to steady-state operating conditions, meaning all fluctuations are about a constant, time-averaged value, and the system is not undergoing any transient changes in operating conditions.

After detecting values of peak frequency and amplitude of oscillation for both inlet and outlet signals, these values are averaged to provide a single peak frequency and amplitude of oscillation for each set of operating conditions.

#### 4.1. Peak frequency of oscillation

Having described how peak frequency of oscillation is determined for each flow condensation case exhibiting a dominant oscillatory mode, it is possible to evaluate key physical factors governing changes in peak frequency across operating conditions. Fig. 10(a)–(c) provide plots of peak frequency of oscillation versus FC-72 mass velocity, inlet quality, exit quality, and time-averaged inlet pressure for vertical upflow, vertical downflow, and horizontal flow, respectively (similar to Fig. 7 for Q Factor).

Fig. 10(a) shows peak frequency values increasing slightly as mass velocity is increased. Changes in inlet quality appear to have little relationship to changes in frequency, although as exit quality increases frequency is seen to increase as well. Recalling the trend seen in Fig. 7(a) which showed Q values decreasing as exit quality increased, Fig. 10(a) implies frequency of peak oscillatory mode increases as the intensity of the oscillatory mode dies out. Inlet pressure appears to have no effect on peak frequency of oscillation.

Fig. 10(b) provides similar plots for results obtained in vertical downflow orientation. Immediately noticeable when comparing results to those obtained for vertical upflow is the significant reduction in peak frequency of oscillation compared to those seen in vertical upflow (with most cases exhibiting  $f_{peak} = 1-5$  Hz in ver-

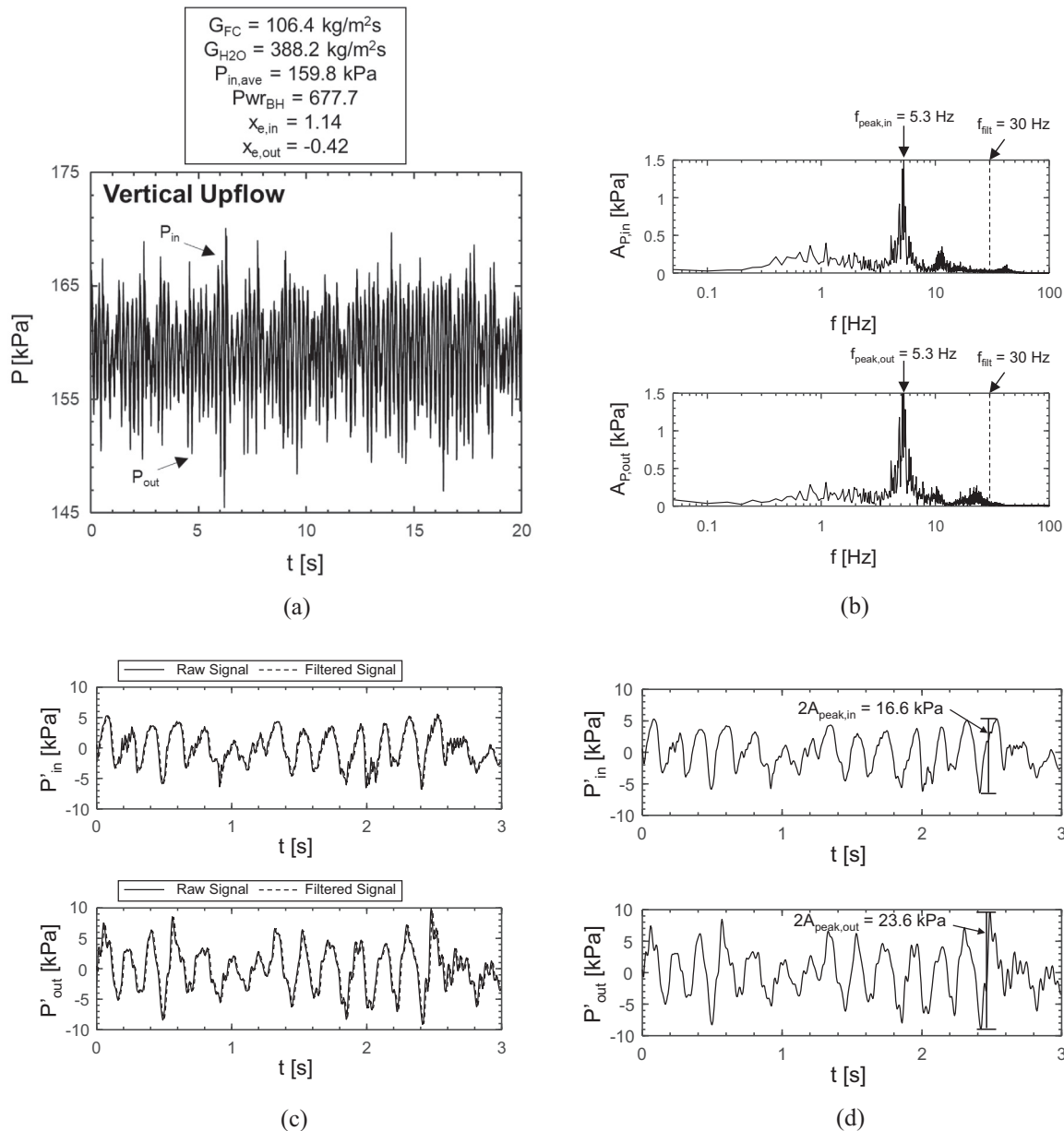


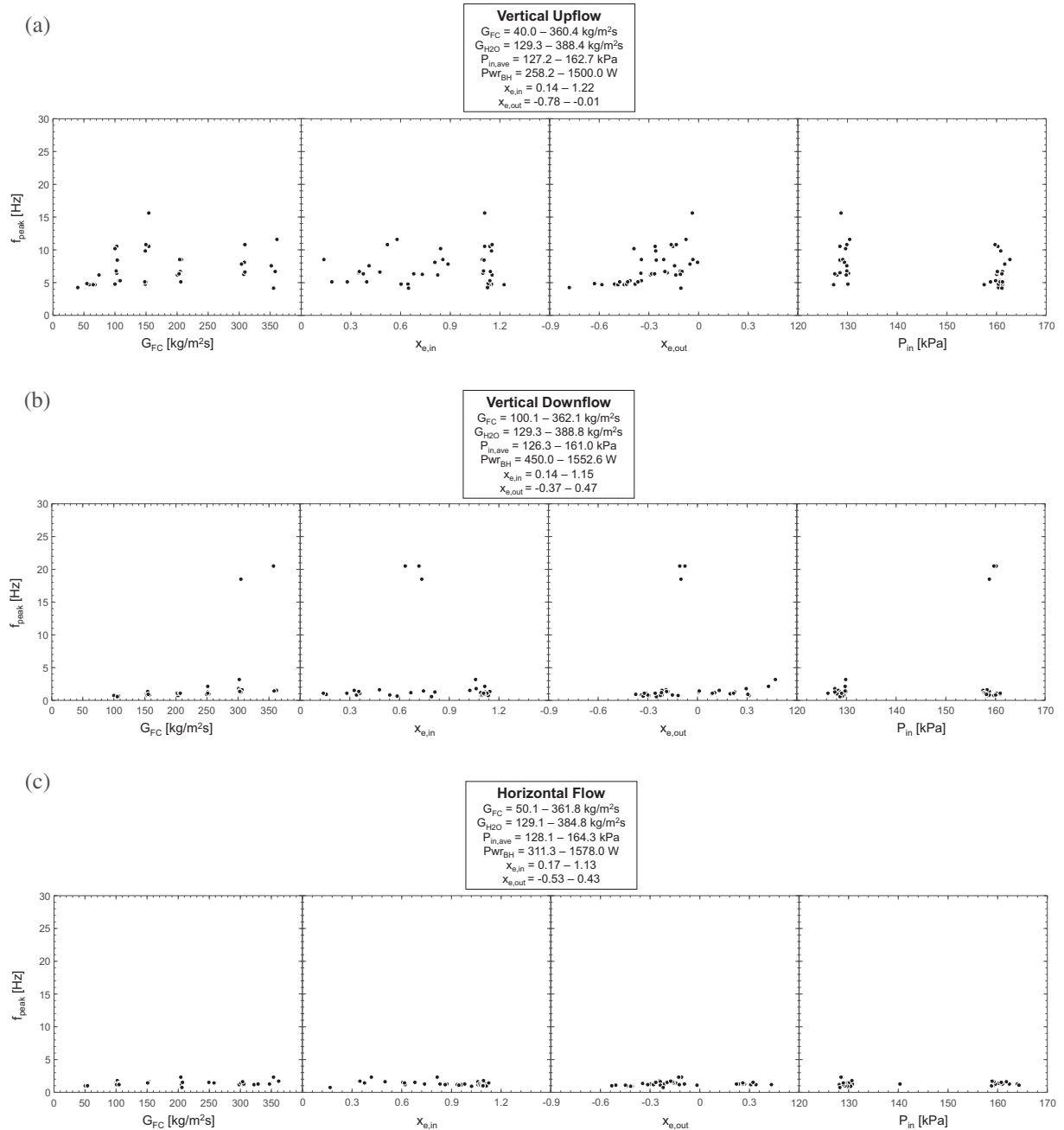
**Fig. 9.** Plots showing detection methodology for peak frequency and amplitude of oscillation: (a) transient FC-72 inlet and outlet pressure signals for entire fast Fourier transform window, (b) associated FFTs with peak frequencies identified, as well as filter frequency (used in later steps) identified, (c) low-pass filtered pressure signals, and (d) amplitude detection using filtered signals.

tical downflow compared to  $f_{peak} = 5\text{--}15 \text{ Hz}$  in vertical upflow). This indicates that at minimum the oscillatory mode observed here is strongly dependent on body force, and possibly that different mechanisms are responsible for oscillatory behavior observed in vertical upflow and downflow orientations (reinforcing the conclusion drawn analyzing respective trends for  $Q$ ).

Analysis of individual plots in Fig. 10(b) again indicates a positive correlation between increases in mass velocity and increases in frequency of oscillation. Trends regarding inlet quality, exit quality, and inlet pressure are largely nonexistent. The presence of three outlier high-frequency measurements seen for high mass velocity, high pressure cases may represent a transition towards a new oscillatory mode for operating conditions not investigated in the current study, but, as sample size for these cases is small, time will not be spent speculating on factors responsible for their presence.

Finally, Fig. 10(c) shows only low frequency oscillations are detected for horizontal flow cases, with no appreciable trends present. This reinforces the idea presented when analyzing Figs. 7 and 8, that oscillations in horizontal flow are of minimal impact compared to those in vertical upflow and downflow orientations.

Fig. 11(a)–(c) provide plots of peak frequency versus the same relevant dimensionless groups used in Fig. 8 for each orientation tested. Fig. 11(a) shows that for vertical upflow peak frequency of oscillation is closely tied to increases in Reynolds, Weber, and Froude numbers calculated based on inlet conditions and vapor properties (see Eqs. (7–9)). Lack of correlation between peak frequency and dimensionless groups calculated based on channel exit conditions and liquid properties reinforces the idea presented when analyzing Fig. 8(a), that oscillatory behavior in vertical upflow orientation is closely tied to vapor flow at the test module inlet.



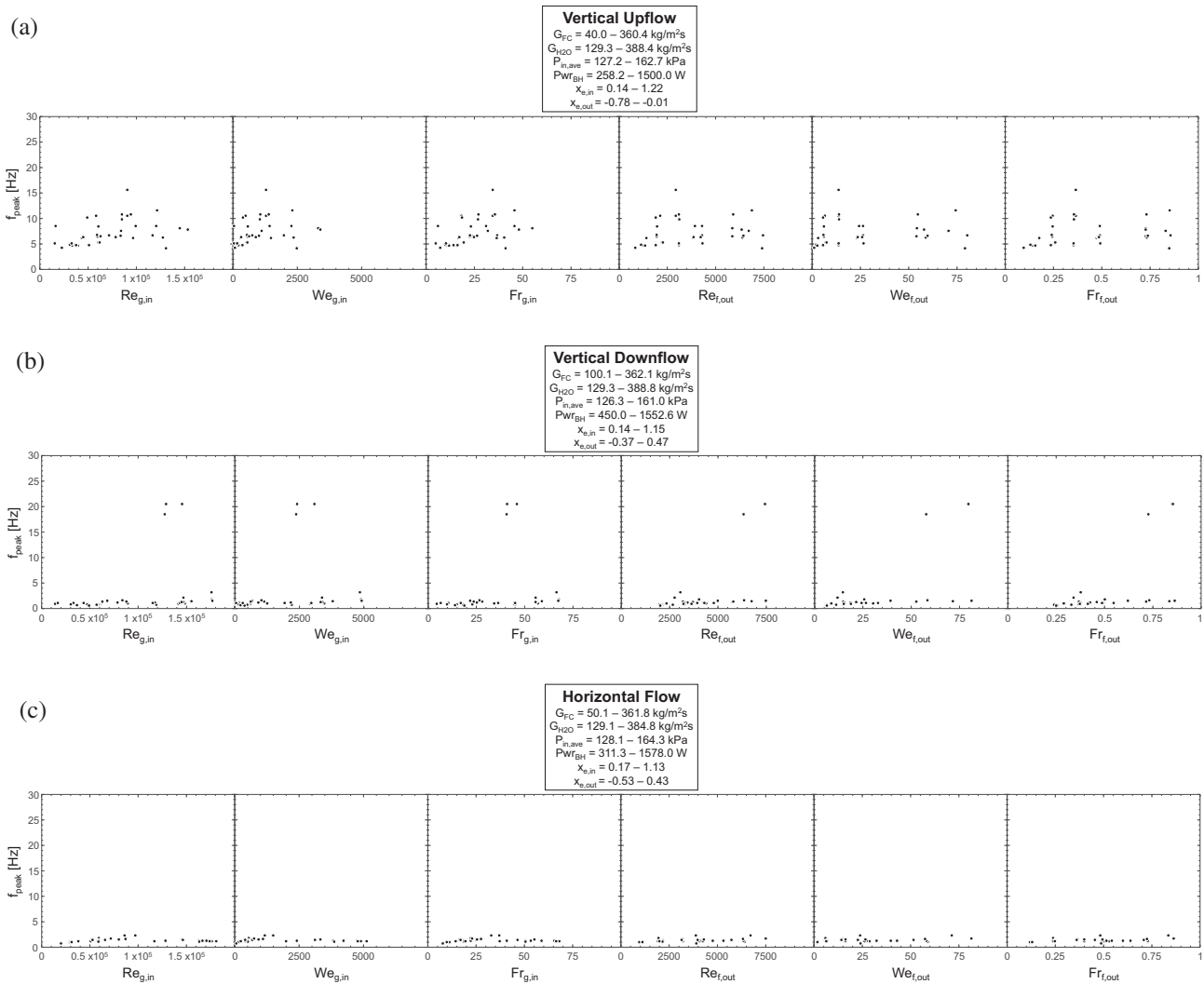
**Fig. 10.** Plots of peak frequency of oscillation versus FC-72 mass velocity, inlet quality, exit quality, and inlet pressure, for all cases in (a) vertical upflow, (b) vertical downflow, and (c) horizontal flow orientations.

Fig. 11(b) provides similar plots for vertical downflow orientation indicating slight positive relationships between peak frequency and dimensionless groups based on both inlet-vapor parameters and exit-liquid parameters. This is an intriguing result, as only parameters based on outlet conditions and liquid properties were shown to govern existence of a peak oscillatory mode in Fig. 8(b). Having eliminated cases with no clear oscillatory mode, Fig. 11(b) indicates peak frequency of oscillation is controlled by a combination of liquid and vapor behavior.

Fig. 11(c) again shows little correlation between changes in operating conditions and differences in peak frequency of oscillation, further differentiating oscillatory behavior observed in horizontal orientation from that in vertical upflow and downflow orientations.

**4.2. Peak amplitude of oscillation**

Similar to Figs. 7 and 10, Fig. 12(a)–(c) provide plots of amplitude versus FC-72 mass velocity, inlet quality, exit quality, and time-averaged inlet pressure for vertical upflow, vertical downflow, and horizontal flow, respectively. Fig. 12(a) shows that amplitude of oscillation for cases in vertical upflow decreases as mass velocity increases, reflecting the trend for Q Factor seen in Fig. 7(a). The highest amplitude cases are all observable for inlet qualities greater than  $x_{e,in} = 1.0$ , although there is not a smooth trend observable in the plot. This is likely due to a change in flow regime along the condensation length associated with higher qualities and low flowrates. Amplitude of oscillation shows a strong dependence on exit quality, decreasing as exit quality increases.



**Fig. 11.** Plots of peak frequency of oscillation versus FC-72 inlet vapor Reynolds, Weber, and Froude numbers, and exit liquid Reynolds, Weber, and Froude numbers, for all cases in (a) vertical upflow, (b) vertical downflow, and (c) horizontal flow orientations.

This matches well with the trend seen in Fig. 7(a), which indicated intensity of the oscillatory mode decreased as exit quality increased. Little variation in amplitude is seen for changes in inlet pressure, indicating mass velocity and exit quality are primarily responsible for governing amplitude of oscillation in vertical upflow.

Fig. 12(b) provides similar plots for vertical downflow orientation. Little variation in amplitude of peak oscillatory mode is seen for changes in FC-72 mass velocity, inlet quality, and inlet pressure, but as exit quality is increased amplitude is seen to decrease. This is likely due to reduced liquid content associated with higher exit quality cases leading to lower intensity (amplitude) pressure oscillations, and reflects a similar trend seen when analyzing changes in  $Q$  value in Fig. 7(b).

Fig. 12(c) provides the first evidence of trends associated with pressure oscillations observed in horizontal orientation, with increases in mass velocity and exit quality leading to clear reductions in amplitude of oscillation, while increases in inlet quality lead to increases in amplitude of oscillation.

Fig. 13(a)–(c) conclude analysis of amplitude trends by providing plots of amplitude of peak oscillatory mode versus relevant dimensionless groups defined in Eqs. (7)–(12) for each orientation. Fig. 13(a), corresponding to tests run in vertical upflow, shows amplitude decreasing for increases in each dimensionless group,

although trends for groups based on inlet conditions and vapor properties are more linear than those based on exit conditions and liquid properties.

Fig. 13(b), corresponding to cases run in vertical downflow orientation, shows amplitude of peak oscillatory mode decreasing for increases in dimensionless groups based on inlet conditions and vapor properties, while no clear trend is present for those based on exit conditions and liquid properties. This is counter to what was seen for both  $Q$  Factor and frequency, both of which exhibited stronger dependence on exit conditions and liquid properties for vertical downflow cases.

Finally, Fig. 13(c) illustrates asymptotic decreases in amplitude of peak oscillatory mode for increases in all dimensionless groups shown. This reinforces the trend first observed in Fig. 12(c), that mass velocity of condensing flow is the key parameter governing changes in amplitude of oscillation for horizontal flow, with other parameters playing a smaller role.

Across the three orientations shown in Figs. 12 and 13 it is notable that vertical downflow exhibits the lowest amplitude oscillations (on average), with low mass velocity cases in horizontal flow providing higher amplitudes than any encountered in vertical downflow, and vertical upflow clearly exhibiting the highest amplitudes of oscillation (on average) for the three orientations.

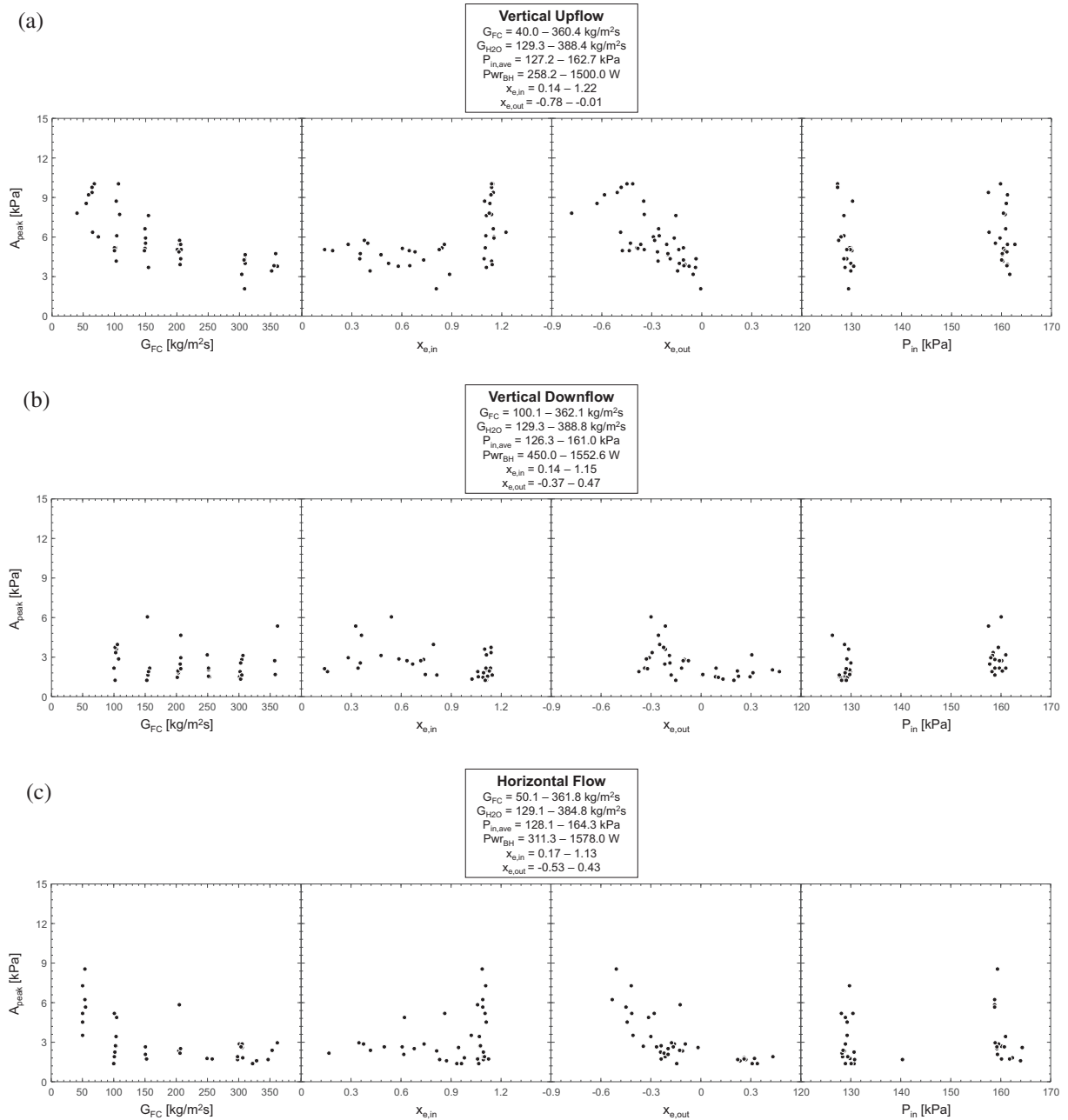


**Fig. 12.** Plots of peak amplitude of oscillation versus FC-72 mass velocity, inlet quality, exit quality, and inlet pressure, for all cases in (a) vertical upflow, (b) vertical downflow, and (c) horizontal flow orientations.

This is reflected in evaluation of peak amplitude ratio for each orientation, defined as

$$Peak \text{ Amplitude Ratio} = \max \left( \frac{A_{peak}}{P_{in,ave}} \right) \times 100\%, \quad (14)$$

which exhibits values of 7.9% for vertical upflow, 3.8% for vertical downflow, and 5.6% for horizontal flow.

Although this contradicts the conclusion drawn from analysis of Q Factor and peak frequency that horizontal flow exhibits the most stable behavior, it is not entirely unexpected due to the role of body force in stabilizing liquid film motion during vertical downflow condensation. It also matches reasonably well with the observations of Soliman and Berenson [65], who saw values of peak amplitude ratio less than 10% for vertical upflow and less than 5% for vertical downflow and horizontal flow orientations.

Having shown that different parameters affect characteristics of oscillatory behavior differently, it is important to recognize the inability of a single parameter to fully characterize oscillatory motion. Only by analyzing trends related to Q Factor (governing the ‘intensity’ of the oscillatory mode), frequency (the rate at which it occurs in time), and amplitude (the degree to which it changes local flow characteristics) together may a full picture of factors governing oscillatory behavior in flow condensation be obtained.

#### 4.3. Impact of oscillatory modes

It is possible to discuss relative impact of oscillatory modes by analyzing their Q Factors, frequencies, and amplitudes together. An oscillatory mode with high values of all three can be said to

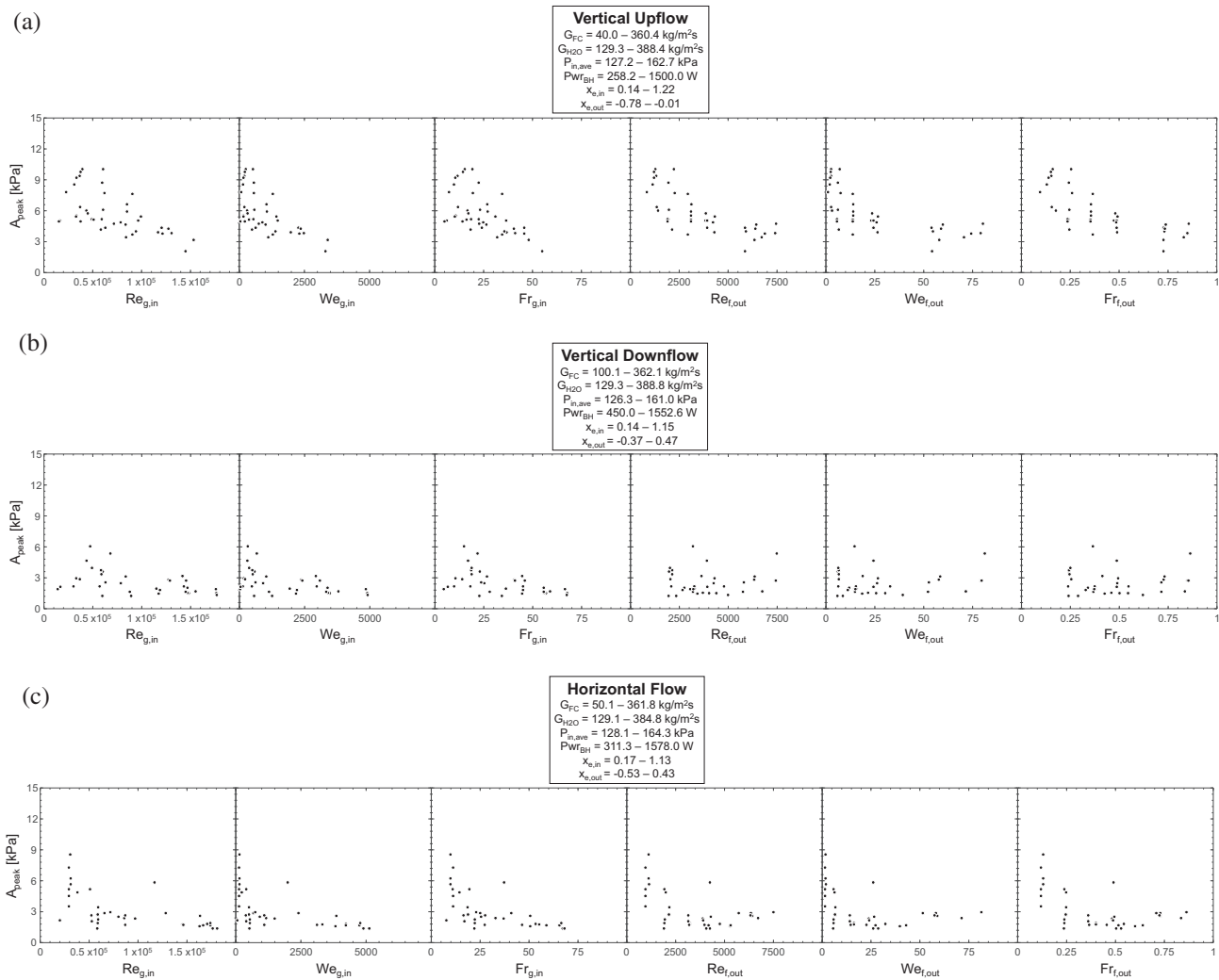


**Fig. 13.** Plots of peak amplitude of oscillation versus FC-72 inlet vapor Reynolds, Weber, and Froude numbers, and exit liquid Reynolds, Weber, and Froude numbers, for all cases in (a) vertical upflow, (b) vertical downflow, and (c) horizontal flow orientations.

(1) be well described by a single frequency and amplitude (due to high  $Q$ ), and (2) exert a relatively large influence on system behavior and performance (due to high frequency and amplitude leading to rapidly changing local pressures). The opposite is true for cases with low values of all three parameters.

Fig. 14(a)–(c) provide plots of peak frequency versus  $Q$  Factor, amplitude of peak oscillatory mode versus  $Q$  Factor, and frequency versus amplitude, respectively, for all orientations tested. Fig. 14(a) shows much wider ranges of both  $Q$  Factor and peak frequency are encountered in vertical upflow orientation compared to vertical downflow (neglecting outlying cases) and horizontal flows. Additionally, a small decrease in frequency is apparent for vertical upflow as  $Q$  increases, indicating lower frequency oscillatory modes may be more well defined. No clear trends are present for vertical downflow and horizontal flow orientations.

Fig. 14(b) indicates that, for both vertical upflow and downflow orientations, higher values of  $Q$  are seen for cases with higher amplitude oscillations. This makes intuitive sense based on how  $Q$  Factor is calculated, as higher amplitude peaks on the frequency response will lead to higher  $Q$  values as well as higher amplitude oscillations observed in pressure signals. The fact that higher  $Q$  leads to higher amplitude in these two cases does not have to be true (e.g., multiple lower and/or distributed peaks could lead to high amplitude with low  $Q$ ), however, and that it indicates oscillatory behavior observed in pressure curves is the result of a single

physical mechanism. The lack of observable trend for horizontal flow, meanwhile, further reinforces the idea that no single, clear mechanism is present behind oscillations observed in this orientation.

Fig. 14(c) shows plots of peak frequency versus amplitude for all three orientations. Vertical upflow once again exhibits the most dynamic (meaning large frequencies and amplitudes of oscillation) behavior, but the lack of trends for each plot indicates factors governing frequency of oscillation are independent from those determining amplitude. This is an important conclusion, as it indicates fundamentally different instability mode from that recently analyzed for flow boiling [81–84].

Overall, trends for key parameters characterizing oscillatory behavior exhibit clear differences for near-identical operating conditions (flow rate, pressure, quality) depending on orientation. Table 2 provides a summary of trends for each combination of key parameter and orientation, as well as general observations about oscillatory behavior observed in each orientation.

## 5. Relationship to observed interfacial behavior

Although analysis of experimental pressure data clearly shows the presence of oscillatory modes in flow condensation, evaluation of their characteristics is incomplete without some commentary on

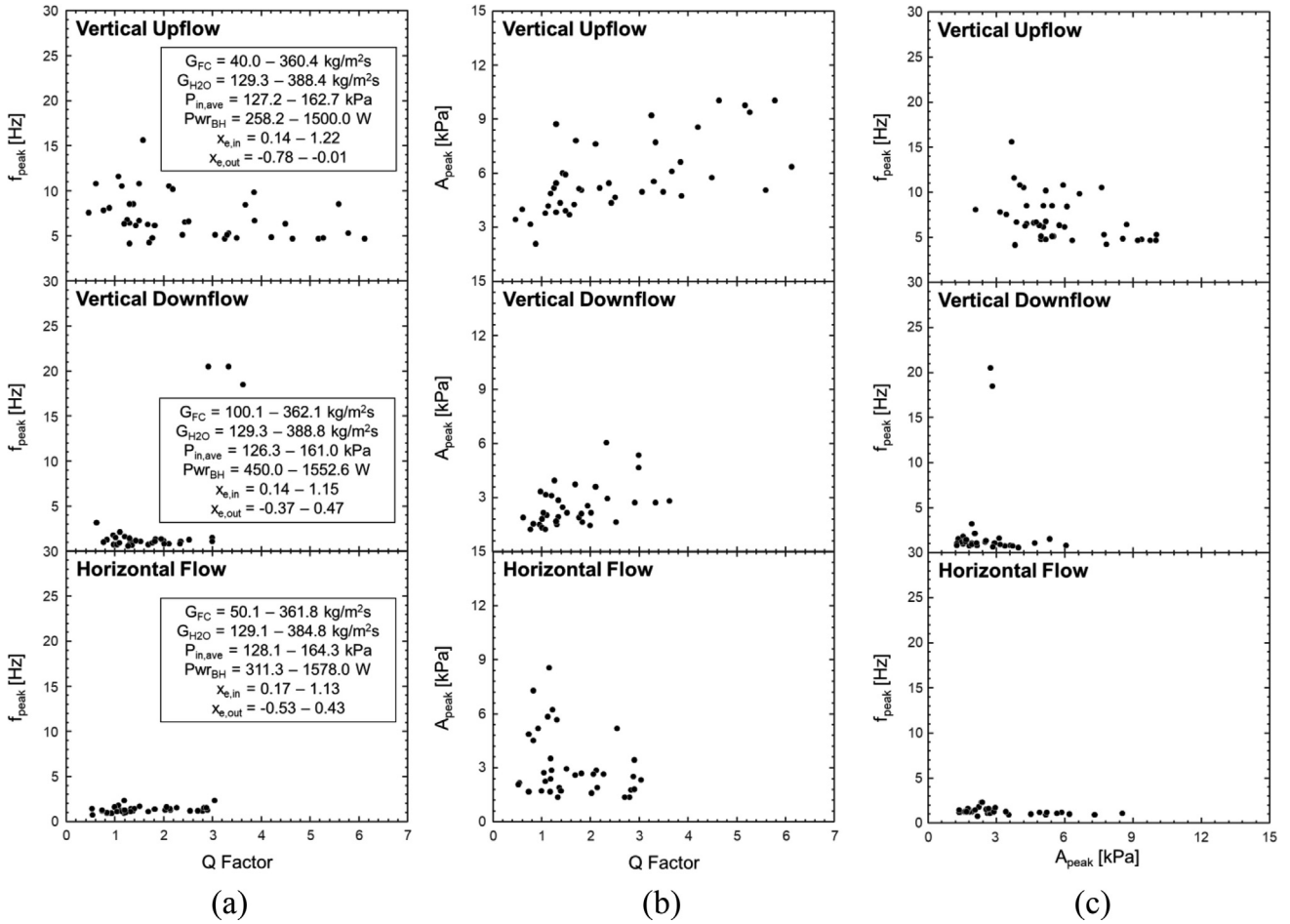


Fig. 14. Plots of (a) peak frequency of oscillation versus Q factor, (b) amplitude of peak oscillation versus Q factor, and (c) peak frequency versus peak amplitude for vertical upflow, vertical downflow, and horizontal flow orientations.

Table 2

Summary of trends governing oscillatory behavior in each orientation.

Parameter	Vertical upflow	Vertical downflow	Horizontal flow
$Q$	<ul style="list-style-type: none"> <li>Decreases with increasing <math>G_{FC}</math>, <math>x_{e,in}</math></li> <li>Strong dependence on inlet vapor conditions, weak dependence on exit liquid conditions</li> </ul>	<ul style="list-style-type: none"> <li>Increases with increasing <math>G_{FC}</math></li> <li>Only exhibits dependence on exit liquid conditions</li> </ul>	<ul style="list-style-type: none"> <li>No clear trends</li> <li>Lowest <math>Q</math> values and highest percentage of <math>Q = 0</math> cases of three orientations</li> </ul>
$f_{peak}$	<ul style="list-style-type: none"> <li>Increases with increasing <math>G_{FC}</math></li> <li>Only exhibits dependence on inlet vapor conditions</li> </ul>	<ul style="list-style-type: none"> <li>Increases with increasing <math>G_{FC}</math></li> <li>Shows slight correlation with inlet vapor and exit liquid parameters</li> </ul>	<ul style="list-style-type: none"> <li>No clear trends</li> <li>Lowest frequency values observed among three orientations</li> </ul>
$A_{peak}$	<ul style="list-style-type: none"> <li>Decreases with increasing <math>G_{FC}</math>, may increase with <math>x_{e,in}</math></li> <li>Dependence on both inlet vapor and exit liquid parameters</li> </ul>	<ul style="list-style-type: none"> <li>Decreases with increasing <math>x_{e,out}</math></li> <li>Only exhibits dependence on inlet vapor parameters</li> <li>Lowest amplitude oscillations of three orientations</li> </ul>	<ul style="list-style-type: none"> <li>Decreases with increasing <math>G_{FC}</math></li> <li>Strong dependence on both inlet vapor and exit liquid parameters</li> </ul>
General Observations	<ul style="list-style-type: none"> <li>Highest percentage of cases exhibiting dominant oscillatory mode, 72%</li> <li>Highest peak amplitude ratio, 7.9%</li> <li>Highest average frequency values</li> <li>Overall, most dynamic orientation</li> </ul>	<ul style="list-style-type: none"> <li>61% of cases exhibiting dominant oscillatory mode</li> <li>Lowest peak amplitude ratio, 3.8%</li> <li>Overall, appreciable dynamic behavior observed, but at low amplitude</li> </ul>	<ul style="list-style-type: none"> <li>Lowest percentage of cases exhibiting dominant oscillatory mode, 54%</li> <li>Moderate peak amplitude ratio, 5.6%</li> <li>Overall, least dynamic behavior observed</li> </ul>

physical mechanisms leading to their formation. Although flow visualization images captured correspond to external flow condensation (as discussed in Section 2) and all results analyzed thus far have been for internal flow, it is expected that key behavior at the interface between liquid film and vapor flow will be similar for the two configurations. Differences in liquid film and interfacial behavior have been discussed in previous work as the key

feature influenced by body force which may lead to differences in condensation behavior [77,78], and it will be analyzed in that context again here.

Fig. 15 presents flow visualization image sequences captured using the condensation module for flow visualization (CM-FV) corresponding to horizontal flow with  $G_{FC} = 82.9 \text{ kg/m}^2\text{s}$ ,  $G_{H_2O} = 696.8 \text{ kg/m}^2\text{s}$ ,  $P_{FC,in} = 123.1 \text{ kPa}$ , and  $x_{e,in} = 1.15$ , with consecutive

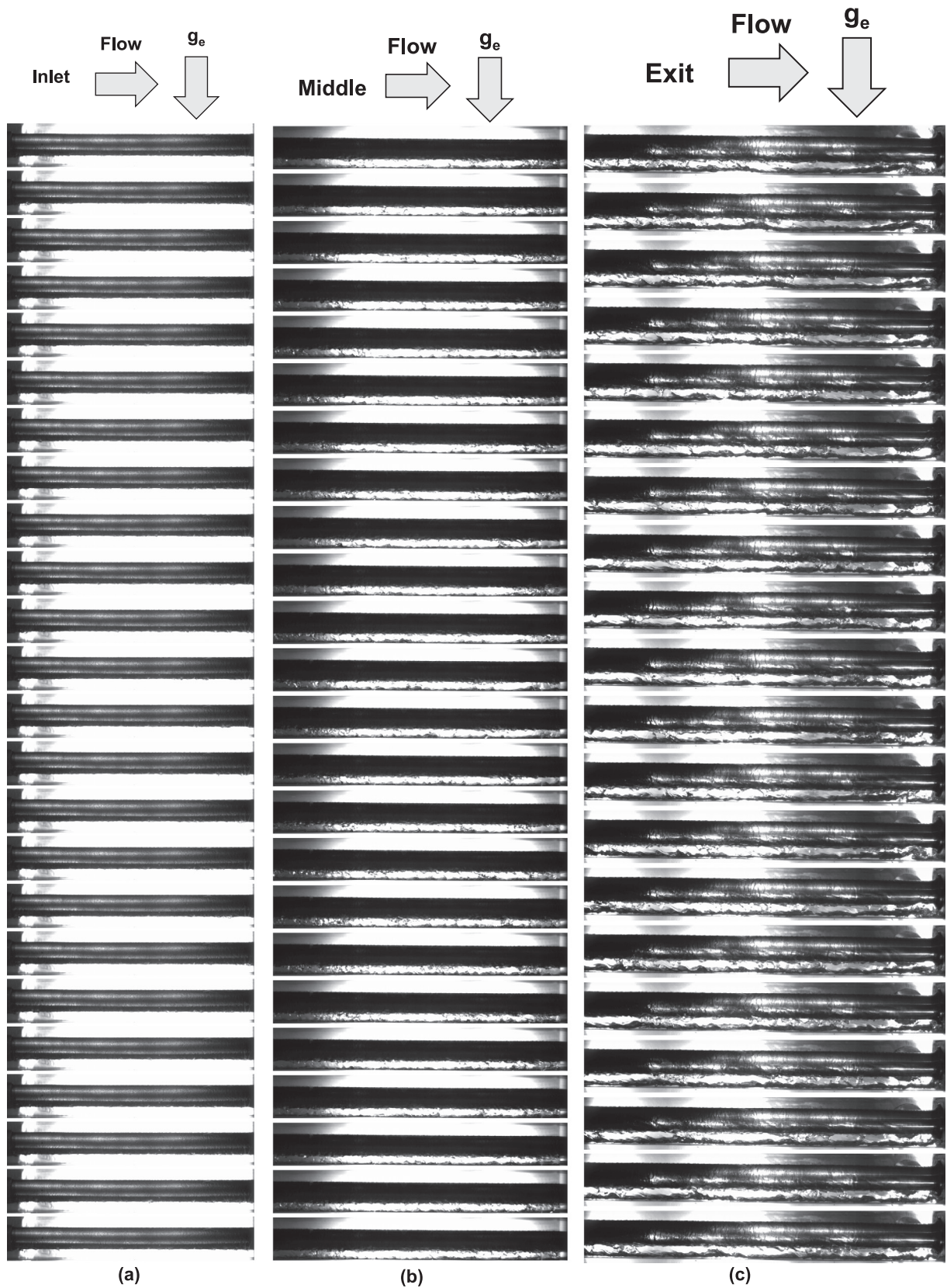


**Fig. 15.** Sequential images of horizontal flow with  $G_{FC} = 82.9 \text{ kg/m}^2 \text{ s}$ ,  $G_{H_2O} = 696.8 \text{ kg/m}^2 \text{ s}$ ,  $P_{FC,in} = 123.1 \text{ kPa}$ ,  $P_{w,BH} = 1361.9$ , and  $x_{e,in} = 1.15$ , centered (a) near the inlet ( $z = 28 \text{ mm}$ ), (b) at the middle of the channel ( $z = 294 \text{ mm}$ ), and (c) near the exit ( $z = 560 \text{ mm}$ ), with individual images in each sequence separated by  $0.0075 \text{ s}$ .

images in each sequence separated by 0.0075 s. Fig. 15(a)–(c) correspond to imaging locations centered near the inlet ( $z = 28$  mm), at the center of the channel ( $z = 294$  mm), and at the channel exit ( $z = 560$  mm), respectively.

Fig. 15(a) shows that, for the case with slightly superheated inlet conditions, a thin liquid film covers the stainless-steel tube (condensation surface) in the upstream portion of the channel. This film shows clear signs of interfacial waves, formed by flow of vapor

in the annulus past liquid. Also important to note is the slight increase in thickness of the liquid film towards the bottom of the stainless steel tube, illustrating gravity's influence on film behavior in horizontal flow, something which becomes more noticeable in later subfigures.

Fig. 15(b) provides similar image sequences, this time captured at the center of the channel. It is apparent that by the time flow reaches the middle of the channel significantly more vapor has

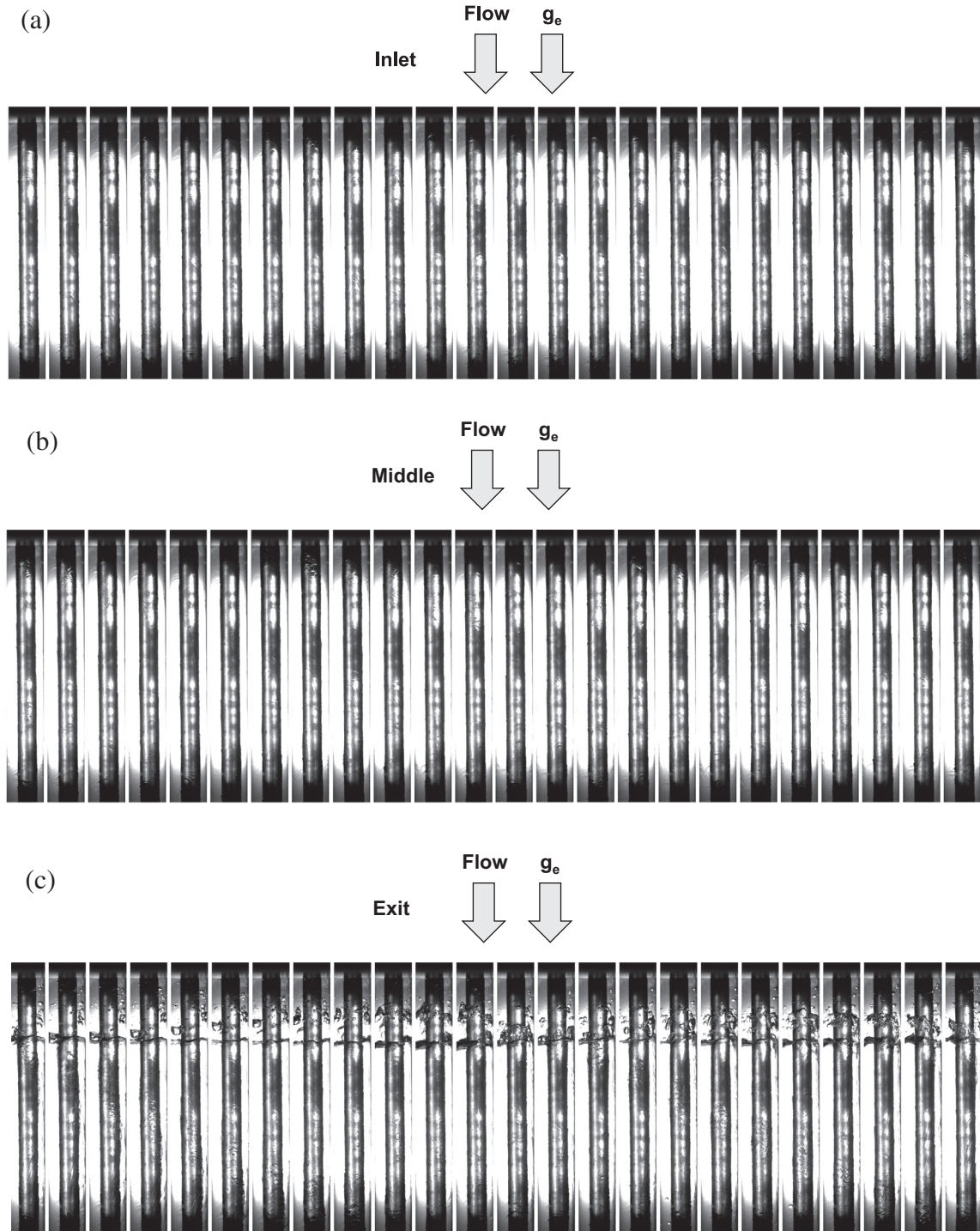
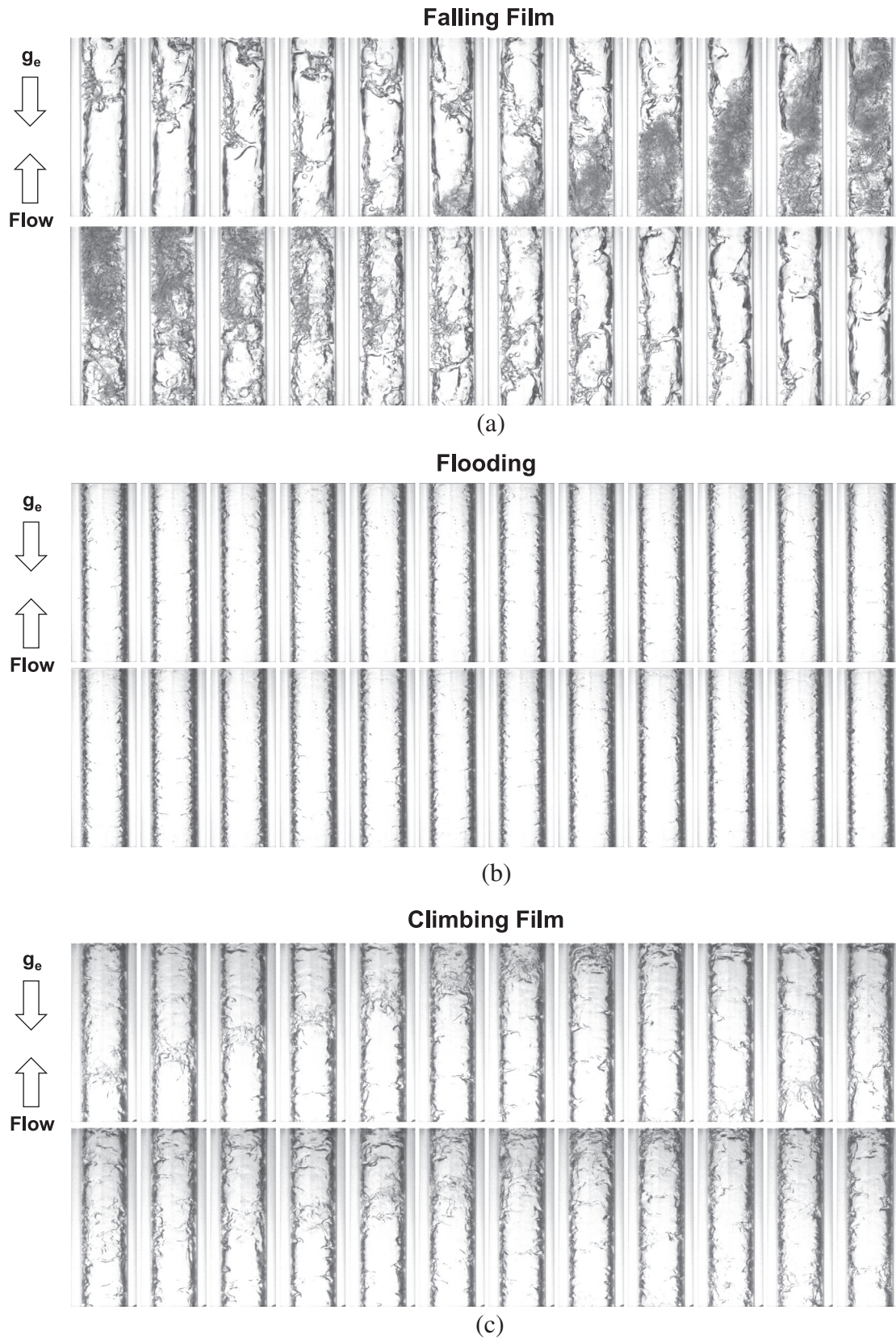


Fig. 16. Sequential images of vertical downflow at the middle region (centered at  $z = 294$  mm) with (a)  $G_{FC} = 34.6$  kg/m<sup>2</sup> s,  $G_{H_2O} = 926.1$  kg/m<sup>2</sup> s,  $P_{FC,in} = 130.1$  kPa,  $P_{WT_{BH}} = 570.3$  W, and  $x_{e,in} = 1.10$ , (b)  $G_{FC} = 33.5$  kg/m<sup>2</sup> s,  $G_{H_2O} = 931.8$  kg/m<sup>2</sup> s,  $P_{FC,in} = 130.5$  kPa,  $P_{WT_{BH}} = 416.7$  W, and  $x_{e,in} = 0.68$ , and (c)  $G_{FC} = 34.2$  kg/m<sup>2</sup> s,  $G_{H_2O} = 934.7$  kg/m<sup>2</sup> s,  $P_{FC,in} = 130.0$  kPa,  $P_{WT_{BH}} = 323.4$  W, and  $x_{e,in} = 0.38$ , with individual images in each sequence separated by 0.0075 s.



**Fig. 17.** Sequential images of (a) falling film in inlet region (centered at  $z = 190$  mm) with  $G_{FC} = 13.32$  kg/m<sup>2</sup> s and  $G_{H2O} = 6.09$  kg/m<sup>2</sup> s, (b) flooding in inlet region with  $G_{FC} = 53.29$  kg/m<sup>2</sup> s and  $G_{H2O} = 73.36$  kg/m<sup>2</sup> s, and (c) climbing film in outer region (centered at  $z = 952$  mm) with  $G_{FC} = 106.45$  kg/m<sup>2</sup> s and  $G_{H2O} = 97.79$  kg/m<sup>2</sup> s, with individual images in each sequence separated by 0.0125 s. Adapted from [40].

condensed into liquid than seen in Fig. 15(a). Due to this liquid buildup and the tendency of body force to drive stratification in horizontal flow (with liquid occupying the bottom of the channel and vapor the top), the liquid film initially formed on the inner stainless steel tube has begun to drop from the tube and occupy the bottom surface of the annulus. Images in Fig. 15(b) clearly show bridging between liquid on the bottom of the inner tube (condensing surface) and the liquid now flowing along the bottom wall of the annulus. Interfacial waves are also clearly visible along both liquid films, indicating the presence of high-velocity vapor flowing between the two.

Fig. 15(c) continues this analysis by providing images captured at the outlet of the channel. Liquid content present in the channel has further increased by this point, with the majority of liquid present at the bottom wall of the annulus, along which large waves appear and flow towards the channel exit.

Across all subfigures shown in Fig. 15, it is apparent that flow dynamic behavior (seen here as interfacial waves, bridging, and film breakup effects) increases as liquid content within the channel increases. Orientation effects in horizontal flow drive stratification of liquid and vapor phases, which leads to the production of interfacial waves, but does not significantly disturb the motion of either liquid or vapor phase, something which is not the case for flow in other orientations.

Fig. 16 provides image sequences for vertical downflow condensation captured at the center ( $z = 294$  mm) of the channel, corresponding to conditions of (a)  $G_{FC} = 34.6$  kg/m<sup>2</sup> s,  $G_{H2O} = 926.1$  kg/m<sup>2</sup> s,  $P_{FC,in} = 130.1$  kPa, and  $x_{e,in} = 1.10$ , (b)  $G_{FC} = 33.6$  kg/m<sup>2</sup> s,  $G_{H2O} = 931.8$  kg/m<sup>2</sup> s,  $P_{FC,in} = 130.5$  kPa, and  $x_{e,in} = 0.68$ , and (c)  $G_{FC} = 34.2$  kg/m<sup>2</sup> s,  $G_{H2O} = 934.7$  kg/m<sup>2</sup> s,  $P_{FC,in} = 130.0$  kPa, and  $x_{e,in} = 0.38$ . The key difference to note across subfigures is the value of inlet quality, decreasing from  $x_{e,in} = 1.10$  in (a), to  $x_{e,in} = 0.68$  in (b), and  $x_{e,in} = 0.38$  in (c). Consecutive images are again separated by 0.0075 s.

Fig. 16(a) shows that, for the case with superheated vapor at the inlet of the channel, little liquid is seen along the stainless-steel tube (condensation surface) at the channel midpoint. What little liquid is present shows signs of interfacial waves, although significantly fewer than were seen in Fig. 15 for horizontal flow.

Fig. 16(b), corresponding to saturated mixture inlet conditions with high quality (low liquid content), exhibits more noticeable interfacial behavior at the channel midpoint due to the larger amount of liquid present within the system. Also important to note is the presence of a small number of liquid droplets entrained in the vapor flow in this case (difficult to observe due to focus of the imaging configuration on capturing interfacial behavior), indicating the increased liquid content within the channel is leading to more dynamic film behavior. It is expected that for higher mass velocities this dynamic behavior would be increased.

Significantly different features are present in Fig. 16(c), corresponding to the lowest inlet quality conditions shown here. Immediately noticeable is the presence of a transition to bulk liquid flow roughly three quarters of the way down the images. Liquid film accumulated along the condensing length is seen to impinge on this solid liquid surface, leading to vapor entrainment within the liquid. Vapor motion within the liquid appears to be largely neutral, likely due to buoyancy force opposing bulk fluid inertia for this entrained vapor.

Although the sharp transition from annular flow condensation along the tube to bulk liquid flow is likely an artifact of the external flow configuration used for CM-FV, and is not expected for internal flow analyzed in CM-HT, the key features of (1) liquid film breakup and droplet impingement, and (2) impact of liquid waves on the solid liquid surface may explain much of the dynamic behavior observed for vertical downflow cases in the preceding sections. The second feature agrees well with the idea proposed by Soliman

and Berenson, that pressure fluctuations observed in horizontal and vertical downflow orientations are due to waves striking the vapor-liquid interface [65].

Flow visualization images corresponding to vertical upflow orientation were not captured using CM-FV due to time constraints on testing, but to present representative behavior for similar operating conditions, Fig. 17 has been adapted from the work of Park and Mudawar [40]. Their work involved investigation of vertical upflow condensation using FC-72 as working fluid in a smooth circular tube with comparable hydraulic diameter and condensation length to that used in the present study. Their original experimental work should be consulted for additional details.

Subfigures in Fig. 17 correspond to cases with slightly superheated inlet conditions and (a)  $G_{FC} = 13.32$  kg/m<sup>2</sup> s and  $G_{H2O} = 6.09$  kg/m<sup>2</sup> s, (b)  $G_{FC} = 53.29$  kg/m<sup>2</sup> s and  $G_{H2O} = 73.36$  kg/m<sup>2</sup> s, and (c)  $G_{FC} = 106.45$  kg/m<sup>2</sup> s and  $G_{H2O} = 97.79$  kg/m<sup>2</sup> s, captured at distances of  $z = 190$  mm,  $z = 190$  mm, and  $z = 952$  mm from the start of the condensation length, respectively. They primarily serve to characterize the impact of increasing mass velocity on liquid film behavior in vertical upflow orientation. This includes *falling film* behavior for very low mass velocities (where body force is much stronger than flow inertia, causing the liquid film to move counter to bulk flow and resulting in significant breakup and entrainment effects), *flooding* at moderate mass velocities (where liquid film is largely stationary), and *climbing film* at high mass velocities (where interfacial shear provided by the fast-moving vapor core is sufficient to overcome body force and advect the liquid film along the channel).

The key takeaway across these three subfigures is the role of increased mass velocity acting to stabilize liquid film behavior in vertical upflow orientation. This matches well with trends seen in Sections 3 and 4, which indicated a strong dependence of flow stability on increased mass velocity in vertical upflow orientation.

Across all three orientations, agreement between parametric trends evaluated in Sections 3 and 4 and conclusions drawn from qualitative analysis of corresponding flow visualization image sequences reveals a strong correlation between measured pressure oscillatory modes and observed liquid film behavior. Future work centering on a more thorough parametric analysis of flow visualization image sequences and simultaneous pressure measurements may lead to establishment of a physical basis for observed oscillatory modes in each orientation.

Important to note at this point is a departure from one of the core ideas proposed by Soliman and Berenson [65], that oscillatory behavior observed in vertical downflow and horizontal flow orientations is due to the same mechanism (wave impact on the liquid-vapor interface). Based on differences observed in parametric trends for  $Q$ ,  $f_{peak}$ , and  $A_{peak}$ , as well as differences in liquid film behavior seen in flow visualization image sequences, it is not clear that oscillatory modes in these two orientations are due to the same mechanism. In fact, analysis performed here indicates the existence of distinct oscillatory modes for each of the three orientations investigated.

## 6. Conclusions

This study examined pressure oscillations observed during flow condensation through a smooth circular tube in vertical upflow, vertical downflow, and horizontal flow orientations. Analysis of instantaneous pressure signals measured at module inlet and outlet locations revealed the presence of dominant oscillatory modes in the moderate (1–20 Hz) frequency range whose intensity exhibited dependence on operating conditions including flow rate, quality, and orientation. Investigation of oscillatory phenomena at other locations within the flow loop revealed modes detected

within the test section could be considered independent of modes introduced at other locations, allowing analysis to proceed considering oscillatory behavior observed in the test section to be physical in nature.

Three key parameters were defined and evaluated to describe observed oscillatory behavior: *Q* Factor (governing existence and intensity of oscillatory modes), frequency, and amplitude. Parametric trends for each were evaluated across a range of relevant operating conditions and interpreted using relevant dimensionless groups. These showed a strong dependence of oscillatory characteristics on orientation. Important qualitative conclusions are summarized in Table 2.

Finally, flow visualization images sequences for vertical upflow, vertical downflow, and horizontal flow orientations were presented, and used to provide commentary on the effects of liquid mass accumulation, inlet quality, and mass velocity in addition to orientation on observed dynamic behavior.

Key conclusions from this study are:

- (1) Flow condensation exhibits a wide range of oscillatory behavior depending on operating conditions and flow orientation. This behavior is seen to be independent of mechanical sources within the flow loop, indicating it is physical in nature.
- (2) Parametric evaluation of *Q* Factor, peak frequency, and amplitude of peak oscillatory mode reveal changes to key operating conditions including mass velocity, inlet quality, and exit quality affect these parameters differently depending on flow orientation. Across the three orientations investigated here, vertical upflow is seen to exhibit the most dynamic behavior, with vertical downflow exhibiting less, and horizontal flow showing the least oscillatory behavior.
- (3) For the most extreme case investigated here, amplitude of oscillation is seen to be 7.9% of time-averaged inlet pressure, indicating pressure oscillations are of sufficiently low magnitude to not impact system safety.
- (4) Analysis of flow visualization image sequences indicates liquid film behavior in each orientation reflecting conclusions drawn regarding overall dynamic behavior. More thorough analysis of interfacial behavior and liquid film dynamics in future work may provide a physical basis for modeling of dominant oscillatory modes in flow condensation.

### Conflict of interest

The authors declared that there is no conflict of interest.

### Acknowledgements

The authors are grateful for financial support provided by the National Aeronautics and Space Administration (NASA) under grant no. NNX17AK98G, and technical support of the NASA Glenn Research Center, Cleveland, Ohio. This work was also supported by NASA Space Technology Research Fellowship NNX15AP29H.

### Appendix A. Supplementary material

Supplementary data associated with this article can be found, in the online version, at <https://doi.org/10.1016/j.ijheatmasstransfer.2018.07.072>.

### References

- [1] I. Mudawar, Assessment of high-heat-flux thermal management schemes, *IEEE Trans. - CPMT* 24 (2001) 122–141.
- [2] C.L. Tien, K.S. Chung, Entrainment limits in heat pipes, *AIAA J.* 17 (1979) 643–646.
- [3] T.J. LaClair, I. Mudawar, Thermal transients in a capillary evaporator prior to the initiation of boiling, *Int. J. Heat Mass Transf.* 43 (2000) 3937–3952.
- [4] M. Shafahi, V. Bianco, H. Vafai, O. Manco, An investigation of the thermal performance of cylindrical heat pipes using nanofluids, *Int. J. Heat Mass Transf.* 53 (2010) 376–383.
- [5] P.J. Marto, V.J. Lepere, Pool boiling heat transfer from enhanced surfaces to dielectric fluids, *J. Heat Transfer* 104 (1982) 292–299.
- [6] I. Mudawar, T.M. Anderson, Parametric investigation into the effects of pressure, subcooling, surface augmentation and choice of coolant on pool boiling in the design of cooling systems for high-power density chips, *J. Electron. Packag.* 112 (1990) 375–382.
- [7] I. Mudawar, T.M. Anderson, Optimization of extended surfaces for high flux chip cooling by pool boiling, *J. Electron. Packag.* 115 (1993) 89–100.
- [8] J.A. Shmerler, I. Mudawar, Local heat transfer coefficient in wavy free-falling turbulent liquid films undergoing uniform sensible heating, *Int. J. Heat Mass Transf.* 31 (1988) 67–77.
- [9] I. Mudawar, R.A. Houpt, Mass and momentum transport in smooth falling liquid films laminarized at relatively high Reynolds numbers, *Int. J. Heat Mass Transf.* 36 (1993) 3437–3448.
- [10] C.O. Gersey, I. Mudawar, Effects of heater length and orientation on the trigger mechanism for near-saturated flow boiling CHF - I. Photographic and statistical characterization of the near-wall interfacial features, *Int. J. Heat Mass Transf.* 38 (1995) 629–642.
- [11] S.M. Ghiaasiaan, *Two-Phase Flow, Boiling and Condensation in Conventional and Miniature Systems*, Cambridge University Press, New York, 2008.
- [12] W. Qu, I. Mudawar, Thermal design methodology for high-heat-flux single-phase and two-phase micro-channel heat sinks, in: *Proc. I-THERM 2002*, San Diego, California, pp. 347–359.
- [13] S. Mukherjee, I. Mudawar, Smart pumpless loop for micro-channel electronic cooling using flat and enhanced surfaces, *IEEE Trans. - CPMT* 26 (2003) 99–109.
- [14] S. Mukherjee, I. Mudawar, Pumpless loop for narrow channel and micro-channel boiling from vertical surfaces, *J. Electron. Packag.* 125 (2003) 431–441.
- [15] J. Lee, I. Mudawar, Critical heat flux for subcooled flow boiling in micro-channel heat sinks, *Int. J. Heat Mass Transf.* 52 (2009) 3341–3352.
- [16] J. Lee, I. Mudawar, Fluid flow and heat transfer characteristics of low temperature two-phase micro-channel heat sinks - part 1: experimental methods and flow visualization results, *Int. J. Heat Mass Transf.* 51 (2008) 4315–4326.
- [17] M. Monde, T. Inoue, Critical heat flux in saturated forced convective boiling on a heated disk with multiple impinging jets, *J. Heat Transf.* 113 (1991) 722–727.
- [18] D.C. Wadsworth, I. Mudawar, Enhancement of single-phase heat transfer and critical heat flux from an ultra-high-flux simulated microelectronic heat source to a rectangular impinging jet of dielectric liquid, *J. Heat Transf.* 114 (1992) 764–768.
- [19] M.E. Johns, I. Mudawar, An ultra-high power two-phase jet-impingement avionic clamshell module, *J. Electron. Packag.* 118 (1996) 264–270.
- [20] I. Mudawar, Recent advances in high-flux, two-phase thermal management, *J. Thermal Sci. Eng. Appl.* 5 (2013) 021012.
- [21] W.P. Klinging, J.C. Rozzi, I. Mudawar, Film and transition boiling correlations for quenching of hot surfaces with water sprays, *J. Heat Treating* 9 (1992) 91–103.
- [22] D.D. Hall, I. Mudawar, Experimental and numerical study of quenching complex-shaped metallic alloys with multiple, overlapping sprays, *Int. J. Heat Mass Transf.* 38 (1995) 1201–1216.
- [23] L. Lin, R. Ponnappan, Heat transfer characteristics of spray cooling in a closed loop, *Int. J. Heat Mass Transf.* 46 (2003) 3737–3746.
- [24] J.D. Bernardin, I. Mudawar, A Leidenfrost point model for impinging droplets and sprays, *J. Heat Transf.* 126 (2004) 272–278.
- [25] M. Visaria, I. Mudawar, Effects of high subcooling on two-phase spray cooling and critical heat flux, *Int. J. Heat Mass Transf.* 51 (2008) 5269–5278.
- [26] I. Mudawar, D. Bharathan, K. Kelly, S. Narumanchi, Two-phase spray cooling of hybrid vehicle electronics, *IEEE Trans. - CPMT* 32 (2009) 501–512.
- [27] M. Visaria, I. Mudawar, Application of two-phase spray cooling for thermal management of electronic devices, *IEEE Trans. - CPMT* 32 (2009) 784–793.
- [28] I. Mudawar, Two-phase micro-channel heat sinks: theory, applications and limitations, *J. Electron. Packag.* 133 (2011) 041002–41012.
- [29] M.K. Sung, I. Mudawar, Experimental and numerical investigation of single-phase heat transfer using a hybrid jet impingement/micro-channel cooling scheme, *Int. J. Heat Mass Transf.* 49 (2006) 682–694.
- [30] M.K. Sung, I. Mudawar, Single-phase hybrid micro-channel/jet impingement cooling, *Int. J. Heat Mass Transf.* 51 (2008) 4342–4352.
- [31] M.K. Sung, I. Mudawar, Single-phase and two-phase heat transfer characteristics of low temperature hybrid micro-channel/micro-jet impingement cooling module, *Int. J. Heat Mass Transf.* 51 (2008) 3882–3895.
- [32] M.M. Chen, An analytical study of laminar film condensation: Part 2 - Single and multiple horizontal tubes, *J. Heat Transf.* 83 (1961) 55–60.
- [33] J.F. Roques, V. Dupont, J.R. Thome, Falling film transitions on plain and enhanced tubes, *J. Heat Transf.* 124 (2002) 491–499.
- [34] Y.T. Kang, H. Hong, Y.S. Lee, Experimental correlation of falling film condensation on enhanced tubes with HFC134a; low-fin and Turbo-C tubes, *Int. J. Refrig.* 30 (2007) 805–811.
- [35] M. Soliman, J.R. Schuster, P.J. Berenson, A general heat transfer correlation for annular flow condensation, *J. Heat Transf.* 90 (1968) 267–274.

- [36] M.K. Dobson, J.C. Chato, Condensation in smooth horizontal tubes, *J. Heat Transf.* 120 (1998) 193–213.
- [37] D. Jung, K. Song, Y. Cho, S. Kim, Flow condensation heat transfer coefficients of pure refrigerants, *Int. J. Refrig.* 26 (2003) 4–11.
- [38] S. Lips, J.P. Meyer, Experimental study of convective condensation in an inclined smooth tube. Part I: inclination effect on flow pattern and heat transfer coefficient, *Int. J. Heat Mass Transf.* 55 (2012) 395–404.
- [39] I. Park, S.M. Kim, I. Mudawar, Experimental measurement and modeling of downflow condensation in a circular tube, *Int. J. Heat Mass Transf.* 57 (2013) 567–581.
- [40] I. Park, I. Mudawar, Climbing film, flooding and falling film behavior in upflow condensation in tubes, *Int. J. Heat Mass Transf.* 65 (2013) 44–61.
- [41] I. Park, H. Lee, I. Mudawar, Determination of flow regimes and heat transfer coefficient for condensation in horizontal tubes, *Int. J. Heat Mass Transf.* 80 (2015) 688–716.
- [42] X. Quan, P. Cheng, H. Wu, Transition from annular flow to plug/slug flow in condensation of steam in microchannels, *Int. J. Heat Mass Transf.* 51 (2008) 707–716.
- [43] S.M. Kim, J. Kim, I. Mudawar, Flow condensation in parallel micro-channels - Part I: experimental results and assessment of pressure drop correlations, *Int. J. Heat Mass Transf.* 55 (2012) 971–983.
- [44] J. Wang, J.M. Li, Theoretical and experimental study of wavy flow during R134a condensation flow in symmetrically and asymmetrically cooled microchannels, *Int. J. Multiph. Flow* 101 (2018) 125–136.
- [45] H. Lee, I. Park, C. Konishi, I. Mudawar, R.I. May, J.R. Juergens, J.D. Wagner, N.R. Hall, H.K. Nahra, M.M. Hasan, J.R. Mackey, Experimental investigation of flow condensation in microgravity, *J. Heat Transf.* 136 (2014) 021502-1–11.
- [46] G. Yadigaroglu, A.E. Bergles, Fundamental and higher-mode density-wave oscillations in two-phase systems, *J. Heat Transf.* 94 (1972) 189–195.
- [47] K. Fukuda, T. Kobori, Classification of two-phase flow instability by density wave oscillation model, *J. Nucl. Sci. Technol.* 16 (1979) 95–108.
- [48] J.-L. Achard, D.A. Drew, R.T. Lahey, The analysis of nonlinear density-wave oscillations in boiling channels, *J. Fluid Mech.* 155 (1985) 213–232.
- [49] Q. Wang, X.J. Chen, S. Kakac, Y. Ding, An experimental investigation of density-wave-type oscillations in a convective boiling upflow system, *Int. J. Heat Fluid Flow* 3 (1994) 241–246.
- [50] V. Pandey, S. Singh, Characterization of stability limits of Ledinegg instability and density wave oscillations for two-phase flow in natural circulation loops, *Chem. Eng. Sci.* 168 (2017) 204–224.
- [51] M. Ozawa, S. Nakanishi, S. Ishigai, Y. Mizuta, H. Tarui, Flow instabilities in boiling channels: Part 1, Pressure drop oscillations, *Bull. JSME* 22 (1979) 1113–1118.
- [52] R.T. Lahey Jr., M.Z. Podowski, On the analysis of various instabilities in two-phase flow, *Multiphase Sci. Technol.* 4 (1989) 183–370.
- [53] V. Jovic, N. Afgan, L. Jovic, D. Spasojevic, An experimental study of the pressure drop oscillations in three parallel channel two phase flow, in: *Proc. Int. Heat Transfer Conf.*, Brighton, UK, 1994, pp. 193–198.
- [54] W.R. Schlichting, R.T. Lahey Jr., M.Z. Podowski, An analysis of interacting instability modes, in a phase change system, *Nucl. Eng. Des.* 240 (2010) 3178–3201.
- [55] K. Fukuda, S. Hasegawa, Analysis on two-phase flow instability in parallel multichannels, *J. Nucl. Sci. Technol.* 16 (1979) 190–199.
- [56] W. Qu, I. Mudawar, Measurement and prediction of pressure drop in two-phase micro-channel heat sinks, *Int. J. Heat Mass Transf.* 46 (2003) 2737–2753.
- [57] H. Lee, I. Park, I. Mudawar, M.M. Hasan, Micro-channel evaporator for space applications - 1. Experimental pressure drop and heat transfer results for different orientations in earth gravity, *Int. J. Heat Mass Transf.* 77 (2014) 1213–1230.
- [58] L.-M. Pan, R.-G. Yan, H.-J. Huang, H. He, P.-F. Li, Experimental study on the flow boiling pressure drop characteristics in parallel multiple microchannels, *Int. J. Heat Mass Transf.* 106 (2018) 642–654.
- [59] J.A. Boure, A.E. Bergles, L.S. Tong, Review of two-phase flow instability, *Nucl. Eng. Des.* 25 (1973) 165–192.
- [60] L. Tadrast, Review on two-phase flow instabilities in narrow spaces, *Int. J. Heat Fluid Flow* 28 (2007) 54–62.
- [61] S. Kakac, B. Bon, A review of two-phase flow dynamic instabilities in tube boiling systems, *Int. J. Heat Mass Transf.* 51 (2008) 399–433.
- [62] L.C. Ruspini, C.P. Marcel, A. Clausse, Two-phase flow instabilities: a review, *Int. J. Heat Mass Transf.* 71 (2014) 521–548.
- [63] W.H. Westendorf, W.F. Brown, Stability of intermixing of high-velocity vapor with its subcooled liquid in cocurrent streams, NASA TN D-3553 (1966).
- [64] J.H. Goodykoontz, R.G. Dorsch, Local heat-transfer coefficients and static pressures for condensation of high-velocity steam within a tube, NASA TN D-3953 (1967).
- [65] M. Soliman, P. Berenson, Flow instability and gravitational effects in condenser tubes, Paper no. Cs. 1.8, in: *Proc. Fourth Int. Conf. on Heat Transfer*, 1970.
- [66] T.J. Rabas, P.G. Minard, Two types of flow instabilities occurring inside horizontal tubes with complete condensation, *Heat Transf. Eng.* 8 (1987) 40–49.
- [67] B.D. Boyer, G.E. Robinson, T.G. Hughes, Experimental investigation of flow regimes and oscillatory phenomena of condensing steam in a single vertical annular passage, *Int. J. Multiph. Flow* 21 (1995) 61–74.
- [68] C.J. Kobus, G.L. Wedekind, B.L. Bhatt, Predicting the onset of a low-frequency, limit-cycle type of oscillatory flow instability in multitube condensing flow systems, *J. Heat Transf.* 123 (2001) 319–330.
- [69] B.L. Bhatt, G.L. Wedekind, A self-sustained oscillatory flow phenomenon in two-phase condensing flow systems, *J. Heat Transf.* 102 (1980) 694–700.
- [70] B.L. Bhatt, G.L. Wedekind, K. Jung, Effects of two-phase pressure drop on the self-sustained oscillatory instability in condensing flows, *J. Heat Transf.* 111 (1989) 538–545.
- [71] G. Liang, N. Mascarenhas, I. Mudawar, Analytical and experimental determination of slug flow parameters, pressure drop and heat transfer coefficient in micro-channel condensation, *Int. J. Heat Mass Transf.* 111 (2017) 1218–1233.
- [72] H. Teng, P. Cheng, T.S. Zhao, Instability of condensate film and capillary blocking in small-diameter-thermosiphon condensers, *Int. J. Heat Mass Transf.* 42 (1999) 3071–3083.
- [73] R. Naik, A. Narain, Steady and unsteady simulations for annular internal condensing flows, part II: instability and flow regime transitions, *Numer. Heat Transfer Part B* 69 (2016) 473–494.
- [74] I. Mudawar, Flow boiling and flow condensation in reduced gravity, *Adv. Heat Transf.* 49 (2017) 225–306.
- [75] H. Lee, C.R. Kharangate, N. Mascarenhas, I. Park, I. Mudawar, Experimental and computational investigation of vertical downflow condensation, *Int. J. Heat Mass Transf.* 85 (2015) 865–879.
- [76] C.R. Kharangate, H. Lee, I. Park, I. Mudawar, Experimental and computational investigation of vertical upflow condensation in a circular tube, *Int. J. Heat Mass Transf.* 95 (2016) 249–263.
- [77] I. Park, L.E. O'Neill, C.R. Kharangate, I. Mudawar, Assessment of body force effects in flow condensation, Part I: experimental investigation of liquid film behavior for different orientations, *Int. J. Heat Mass Transf.* 106 (2017) 295–312.
- [78] L.E. O'Neill, I. Park, C.R. Kharangate, V.S. Devahdhanush, V. Ganesan, I. Mudawar, Assessment of body force effects in flow condensation, part II: criteria for negating influence of gravity, *Int. J. Heat Mass Transf.* 106 (2017) 313–328.
- [79] S.M. Kim, I. Mudawar, Universal approach to predicting two-phase frictional pressure drop for adiabatic and condensing mini/micro-channel flows, *Int. J. Heat Mass Transf.* 55 (2012) 3246–3261.
- [80] S.M. Kim, I. Mudawar, Universal approach to predicting heat transfer coefficient for condensing mini/micro-channel flow, *Int. J. Heat Mass Transf.* 56 (2013) 238–250.
- [81] L.E. O'Neill, C.R. Kharangate, I. Mudawar, Time-averaged and transient pressure drop for flow boiling with saturated inlet conditions, *Int. J. Heat Mass Transf.* 103 (2016) 133–153.
- [82] L.E. O'Neill, I. Mudawar, M.M. Hasan, H.K. Nahra, B. Ramaswamy, N.R. Hall, A. Lokey, J.R. Mackey, Experimental investigation into the impact of density wave oscillations on flow boiling system dynamic behavior and stability, *Int. J. Heat Mass Transf.* 120 (2018) 144–166.
- [83] L.E. O'Neill, I. Mudawar, M.M. Hasan, H.K. Nahra, B. Ramaswamy, J.R. Mackey, Experimental investigation of frequency and amplitude of density wave oscillations in vertical upflow boiling, *Int. J. Heat Mass Transfer* 125 (2018) 1240–1263.
- [84] L.E. O'Neill, I. Mudawar, Mechanistic model to predict frequency and amplitude of density wave oscillations in vertical upflow boiling, *Int. J. Heat Mass Transf.* 123 (2018) 143–171.
- [85] Y. Wei, N. Chen, Square wave analysis, *J. Math. Phys.* 39 (1998) 4226–4245.
- [86] "SciPy v0.14.0 Reference Guide, Signal processing, [scipy.signal.butter](https://docs.scipy.org/doc/scipy-0.14.0/reference/generated/scipy.signal.butter.html)", The scipy community (2014), accessed March 2018, <<https://docs.scipy.org/doc/scipy-0.14.0/reference/generated/scipy.signal.butter.html>>.
- [87] S.W. Chen, T. Hibiki, M. Ishii, M. Mori, F. Watanabe, Experimental investigation of void fraction variation in subcooled boiling flow under horizontal forced vibrations, *Int. J. Heat Mass Transf.* 115 (2017) 954–968.